Machine-Learning Based Optimization for Double-Layer Planar Spiral Coil Design in High-Frequency Wireless Power Transfer Systems

Kanokporn Sukphan

A thesis
submitted in partial fulfillment of the
requirements for the degree of

Master of Science

University of Washington

2024

Committee:

Jungwon Choi

June Lukuyu

Program Authorized to Offer Degree:

Electrical and Computer Engineering

University of Washington

Abstract

Machine-Learning Based Optimization for Double-layer Planar Spiral Coil Design in High-Frequency Wireless Power Transfer Systems

Kanokporn Sukphan

Chair of the Supervisory Committee:
Jungwon Choi
Electrical and Computer Engineering

In Wireless Power Transfer (WPT) systems, the performance with high-frequency in the MHz range depends on several major parts of the system, for example, switching losses of the inverter, the quality factor (Q) of the transmitter and receiver coil for WPT system. Minimized switching losses offer higher efficiency for the inverter. Furthermore, the higher Q of the coil implies higher efficiency. Therefore, it is necessary to improve their performance to achieve a higher efficiency of the overall WPT system, which can be applied in electric vehicles (EVs), unmanned aerial vehicles (UAVs), and drones. This paper presents the optimization of self-resonant coil design in a two-layer planar spiral structure using the machine learning method in the high-frequency WPT system for small and lightweight applications such as drones. Firstly, a deep feed-forward neural network (D-FFNN) model is trained for Q estimation. The training strategies, such as weight initialization, K-fold cross-validation, and hyper-parameter tuning, are adopted to improve the model performance, represented for Q-factor prediction accuracy. Then, optimizing the coil design is approached to explore the optimal design geometric parameters with the high Q. This is done using the APOPT algorithm to solve the mixed integer nonlinear programming problem for high-Q double-layer spiral coil design with the constrained design requirement and resonant condition. Lastly, the coil prototype is implemented for high efficiency, achieving 777.53 of Q with a 20-cm outer diameter, 0.5-mm thickness of the coil, and 3.38-mm thickness of the dielectric layer and operating at 13.56MHz from the proposed method's design suggestion.

Contents

1 Introduction 1

2 Background and Motivation 6

2.1 High-frequency Resonant Inverter using Wide Bandgap Device 6

2.2 High-frequency Double-Layer Spiral Coil Design 12

2.3 Motivation for Machine Learning-Based Coil Design 16

3 Machine Learning-Based Quality Factor Estimation of the High-frequency Coil Design 18

3.1 Deep Learning Technique for High-frequency Coil Designs 19

3.2 Data Collection for the High-frequency Coil Designs 23

3.3 Deep Learning Model Training Methodology 24

3.3.1 Weight Initialization 24

3.3.2 Training, Validation, and Testing Dataset 25

3.3.3 K-fold Cross Validation and Hyper-parameter Tuning 26

3.4 Model Training and Performance Evaluation 27

4 Optimization of the High-frequency Coil Design 31

4.1 Optimization Algorithms 31

4.2 Proposed-Coil Optimization Problem with APOPT Solving Algorithm 33

4.3 Observation on the Proposed Coil Optimization 36

5 Experimental Results 38

5.1 13.56 MHz Frequency Class Φ_2 Inverter Design 38

5.2 13.56 MHz Double-Layer Planar Spiral Coil Design 41
5.2.1 Quality Factor of the Optimized Coil Design using Machine Learning 42
5.2.2 Quality Factor of Coil Design Experiments 42
5.2.3 Comparison of Simulation-based, ML-based and Physical Experiments 44

6 Conclusion and Future Work 47

List of Figures

1.1 Global UAV market between 2023 and 2029 [13]. 1

1.2 Review of different technologies in the WPT system. 3

1.3 High-frequency WPT System Diagram. 3

1.4 Four Basic Topologies of Compensation Networks (a) Series-series (SS); (b) series-parallel (SP); (c) parallel-series (PS); and (d) parallel-parallel (PP). [16] 4

2.1 Class E Inverter. 7

2.2 Class Φ_2 Inverter. 7

2.3 Summary of Si, SiC, and GaN relevant material properties. 9

2.4 Characteristics of output capacitance in GS66508T [4]. 10

2.5 Classification of SR Coil (a) Adjacent turns; (b) Parallel plates; and (c) Coaxial capacitance on turns. [8] 12

2.6 Uniform two-layer spiral coil structure. 13

3.1 Basic neural network architecture. 20

3.2 A Deep Feedforward Neural Network (D-FFNN) with 13 input neurons, two hidden layers, and one output. 21

3.3 K-fold Cross-validation diagram with five folds. 27

3.4 A pre-trained model with 64 batch size and 0.01 learning rate over 500 epochs. 28

3.5 A post-trained model with 64 batch size and 0.001 learning rate over 1000 epochs. 30

4.1 Optimization Algorithm Chart Diagram. 32

4.2 Block diagram for quality factor estimation and double-layer spiral coil design optimization. 33

5.1 Circuit diagram of a 300-W Class 2 inverter with a 160 V DC input voltage, featuring a 300 nH L_F, a 918.4 nH L_{MR}, a 37.5 pF C_{MR}, and a 240 pF parallel capacitor, including a 65 pF C_{OSS} on the input side. It also includes a 363.36 nH L_S and a 4 nF C_S, designed to operate with a 50 Ω load using a GS66508T eGAN FET switching device in LTspice. 38

5.2 Bode plot of Z_{DS}. 39

5.3 Simulation and waveforms of V_{DS} and V_{out}. 41

5.4 Uniform two-layer planar spiral coil design. 43

5.5 A double-layer spiral coil experiment setup. 44

5.6 Magnitude of Z-parameter frequency sweep in the coil design of 2.37-mm of d. 45

5.7 Magnitude of Z-parameter frequency sweep in the coil design of 3.38-mm of d. 45

List of Tables

2.1 Design parameters for coil simulation. 13

3.1 Data collection for the training model. 23
3.2 Quality Factor Evaluation from Different Testing Datasets. 29

5.1 Class Φ_2 inverter performance in three fine-tuning experiments. . . . 40
5.2 Parameter Setup of ANSYS Simulation. 41
5.3 Two-layer spiral coil geometric parameters. 43
5.4 Optimization Results of a double-layer planar spiral coil designs. . . . 46

Chapter 1

Introduction

Nowadays, the development of wireless power transfer is rapidly evolving, including electric vehicles (EVs) and unmanned aerial vehicles (UAVs), including drones, which are a small type of UAVs. The global market of UAVs, also called drones, is expected to grow from USD 30.2 billion in 2024 to USD 48.5 billion in 2029, accounting for 9.9% of CAGR market growth globally [13], as shown in Fig. 1.1.

Traditionally, these types of transportation have relied on cable-based charging systems, which require physical connectors. This provides some drawbacks, such as inconvenience, low flexibility, and reduced efficiency due to contact resistance and mechanical losses. Therefore, wireless power transfer (WPT) systems offer a com-

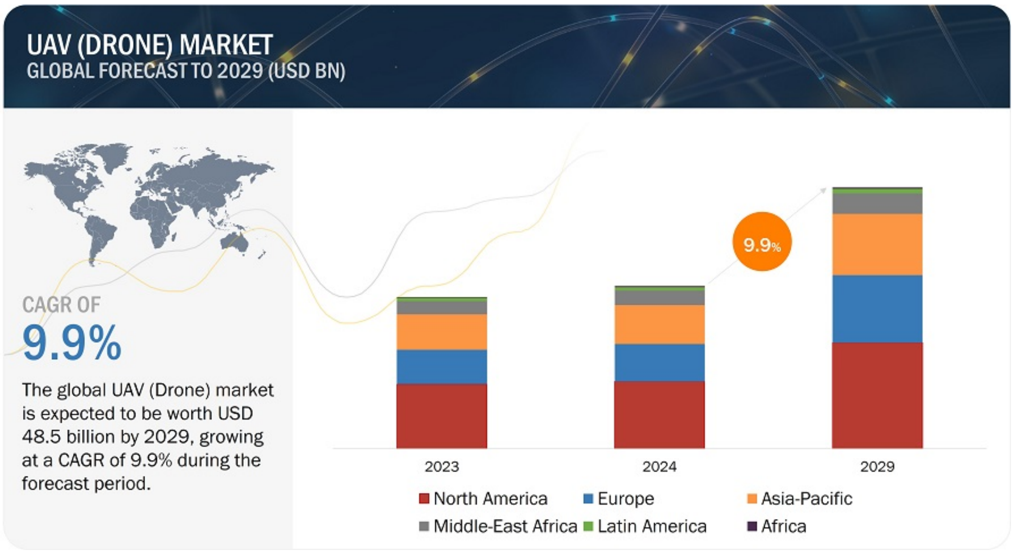

Figure 1.1: Global UAV market between 2023 and 2029 [13].

pelling alternative to traditional cable chargers and also provide several advantages, including greater convenience, reduced maintenance, and the potential for enhanced efficiency. EVs and UAVs are typically powered by batteries, which offer a reduction of carbon footprint instead of using fossil fuel sources. They can also serve military and civilian purposes such as delivery, monitoring, and inspection. Due to increasing demands for UAVs, the requirements of UAV design are apparently compact, lightweight, and highly efficient. Therefore, improving efficiency and high power transfer performance is critical to suit the applications. However, achieving optimal performance in high-frequency WPT systems, particularly at high frequencies, remains a significant technical challenge, such as power losses in semiconductor devices and designing power transmission coils.

To deliver power in a wireless power transfer system, electromagnetic (EM) energy is transmitted between two locations from a power source to an elective load without any physical contact. WPT can be classified into radiative and non-radiative based on the energy transfer mechanism. Radiative power transfer emits EM waves through a vacuum or air medium by an antenna, which usually operates at very high frequencies for a kilometer-range distance, leading to low efficiency. On the other hand, short-range and mid-range applications tend to use a non-radiative WPT mechanism distributed by two application ranges: near-field inductive coupling and magnetic resonant coupling mechanism, respectively, based on the principles of Nikola Tesla [15].

Overall, the WPT system can be applied in wide operating frequencies with different technologies for various applications, as shown in Fig. 1.2 [17]. However, the magnetic inductive coupled system has poor efficiency because it is sensitive to magnetic coupling due to axial and angular misalignment between primary and secondary coils. To overcome this issue, applying a compensation circuit on each coil in the resonant coupling system is encouraged, efficiently operating in a more extended distance application by using two resonators tuned at the same resonant frequency [15].

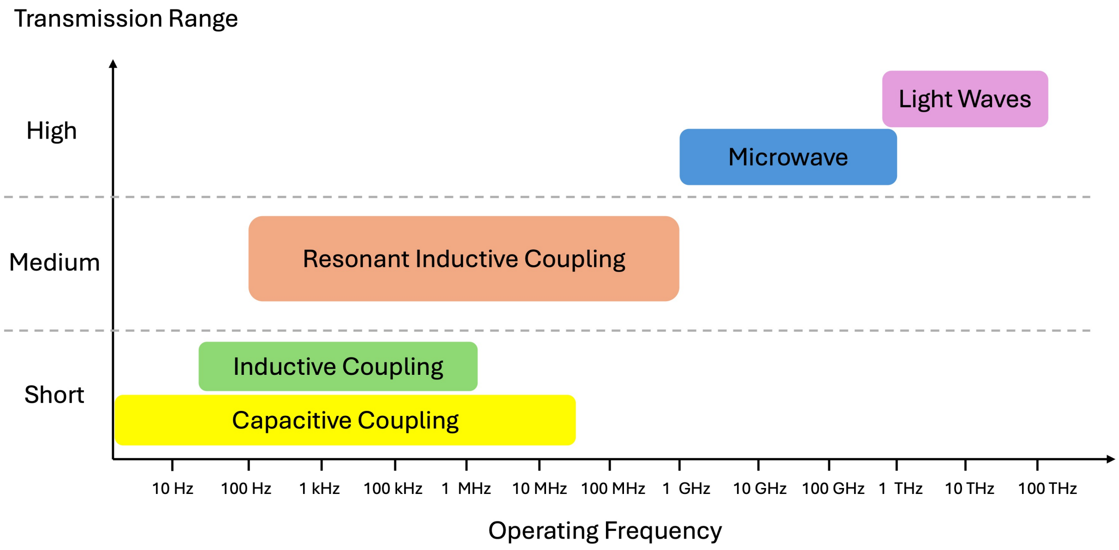

Figure 1.2: Review of different technologies in the WPT system.

Generally, the resonant coupling WPT model consists of the inverter, which can convert constant voltage into a direct current (DC) source to alternating current (AC) voltage. AC voltage allows electromagnetic energy to be generated and exchanged between the transmitter (Tx) and receiver (Rx) coils. The power is delivered through the EM fields between the coils and rectified to DC voltage for electric loads, as presented in Fig. 1.3.

Also, to improve the power transfer performance in the system, the compensation network generates and makes recompense for mutual inductance (M) and coil leakage inductance both in the primary and secondary resonant circuits at the resonant frequency [16]. Compensation networks have four basic compensation topologies, namely the series-series (SS), series-parallel (SP), parallel-series (PS), and parallel-

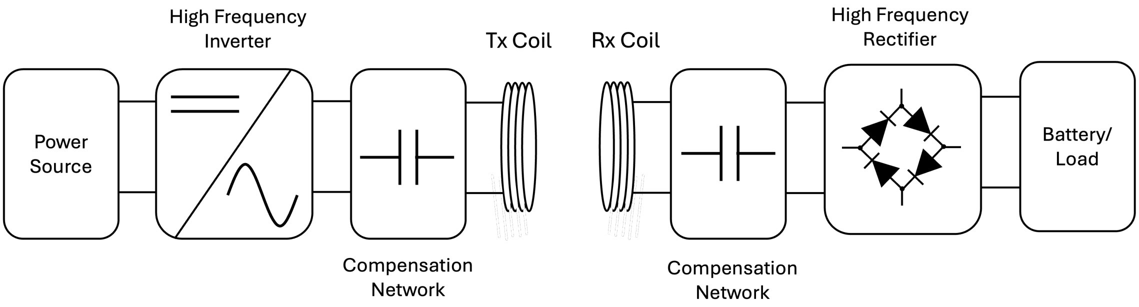

Figure 1.3: High-frequency WPT System Diagram.

parallel (PP) topologies [15] [16], as shown in Fig. 1.4.

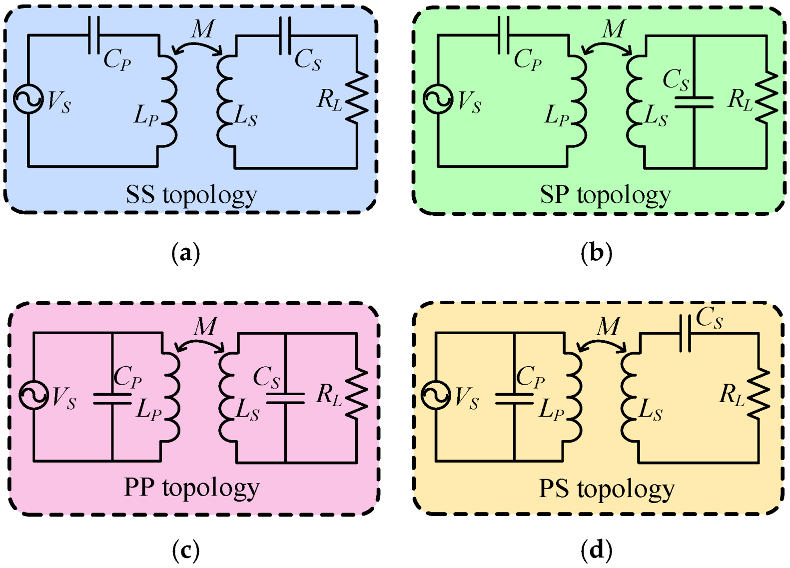

Figure 1.4: Four Basic Topologies of Compensation Networks (a) Series-series (SS); (b) series-parallel (SP); (c) parallel-series (PS); and (d) parallel-parallel (PP). [16]

The performance of the WPT system can also be evaluated by two parts in this research: (i) high efficiency of the inverter/rectifier and (ii) high-quality factor (Q). Firstly, the efficiency can be evaluated by averaged output power over averaged input power depending on switching losses and conduction losses in switching devices and passive components in the inverter/rectifier with a small size. Secondly, the quality factor (Q) is the ratio between the coil's self-inductance and internal resistance. The high Q describes the high transmission performance of a coil design. However, achieving high Q at high frequency is challenging due to the proximity effect, skin effect, and high parasitic capacitance. Specifically, the proximity effect and skin effect cause eddy currents in nearby conductors from alternating magnetic fields that current flowing through the coil. Also, [6] addressed the issue of higher parasitic capacitance (C_p) in the coils. This increases AC resistance, decreasing the Q-factor. Another issue is the limitation of increasing the inductance in the coil. Selecting the small series capacitance (C_s) needed for series compensation at a specific frequency can lead to high peak voltages across C_s, potentially causing breakdown [6]. In addition, the limitation of the design is determined based on target applications that are supposed to be compact and lightweight for drones and small UAVs. Despite standard self-resonant coil designs such as circular and spiral designs, the two-layer planar spiral coil is recommended in [6, 7].

This research generally aims to design a high-Q coil for high-frequency WPT systems. Designing resonant planar spiral coil is approached by machine learning-based quality factor estimation in high-frequency operation, offering integration of machine learning methods and design optimization. Furthermore, it is essential to build experimental design models with the highest quality factors from the proposed method to reach the design goal of compact and lightweight application.

Chapter 2

Background and Motivation

2.1 High-frequency Resonant Inverter using Wide Bandgap Device

In high-frequency WPT systems, applying a resonant inverter is a beneficial topology to enhance a high-efficiency system. This allows the inverter to achieve zero-voltage switching (ZVS) when the switching device turns on or off at zero voltage from the overlap between voltage and current during the switching transition. This condition reduces the voltage stress in switching devices at high-frequency operation. There are several topologies of inverters for high-frequency applications, for example, Class E and Class Φ_2 inverters, consisting of a single switching device. Even though the mentioned inverters are popularly used in high-frequency wireless power transmission because of their compact design and high efficiency from being able to achieve ZVS condition, Class E inverter has considerable switching voltage stress of almost four times the input voltage compared to only approximately two times of input voltage in Class Φ_2 inverter [2].

Therefore, this research focuses on the topology of Class Φ_2 inverter utilizing GS66508 eGaN FET switching devices for a hundred-watt range of output power applications such as drones and small UAVs. Generally, the Class Φ_2 inverter is similarly constructed with the Class E inverter but the Class Φ_2 has additional

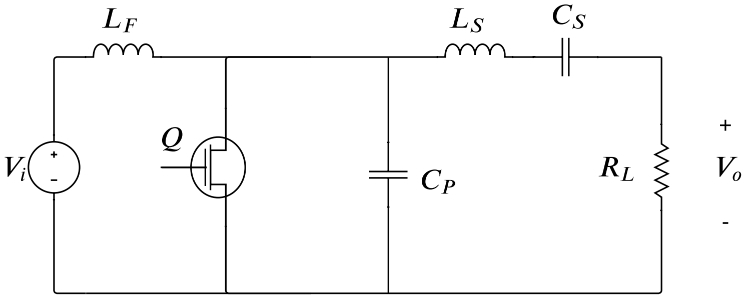

Figure 2.1: Class E Inverter.

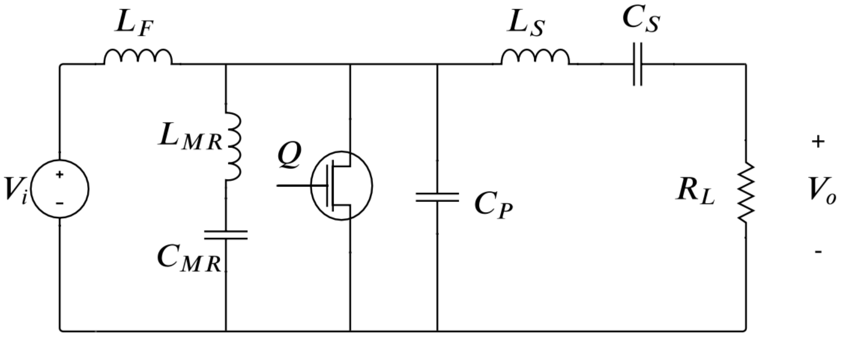

Figure 2.2: Class Φ_2 Inverter.

inductance (L_{MR}) and capacitance (C_{MR}) in parallel with the switching device, as shown in Fig. 2.1 and Fig. 2.2. The difference is responsible for lowering the switch peak voltage by only approximately two times the input voltage in the Class Φ_2 inverter but by four times the input voltage in the Class E inverter. This allows the inverter to operate at higher input voltage and higher efficiency [2] [3]. Therefore, this research focuses on the topology of Class Φ_2 inverter utilizing GS66508 eGaN FET switching devices for a hundred-watt range of output power applications such as drones and small UAVs.

In high-frequency WPT systems, applying a resonant inverter is a beneficial topology to enhance a high-efficiency system. This allows the inverter to achieve zero-voltage switching (ZVS) and reduce the voltage stress of switching devices at high-frequency operation. There are several topologies of inverters for high-frequency applications, for example, Class E and Class Φ_2 inverters, which both offer lower switching voltage stress by consisting of a single switching device. Even though the mentioned inverters are popularly used in high-frequency wireless power transmission because of their compact design and high efficiency from being able to achieve ZVS condition, Class E inverter has considerable switching voltage stress of four times the input voltage compared to only approximately two times of input voltage in Class Φ_2 inverter [2].

In addition, power semiconductor devices are the main indicators of inverter performance based on semiconductor materials and their properties. Also, to operate in the megahertz (MHz) range of frequencies, which can lead to substantial switching losses, it is more efficient to apply inverters with wide-bandgap (WBG) switching devices such as Silicon Carbide (SiC) and Gallium Nitride (GaN). These potential materials have different characteristics on different operating conditions and are classified into properties of high voltage operation, high-frequency switching operation, and high-temperature application. The tradeoffs between the operation conditions are presented in five characteristics: electric field, energy gap, electron velocity, thermal conductivity, and melting point [18] [19]. Also, WBG devices can reach higher switching frequencies and have lower parasitic capacitance than Si material devices because of their higher electron saturation velocity.

Moreover, WBG devices have low switching loss due to lower on-resistance and conduction loss for a broader range of blocking voltages and frequencies. Since WBG materials have wider energy bandgap and lower leakage current, they can operate in high-temperature operation [18]. As the characteristics are shown in Fig. 2.3, WBG devices have benefits over Si-based devices in high-voltage and high-frequency applications, including the high-temperature condition and compact size [18].

Characteristics of GaN devices from a high electron density channel as known as 2-dimensional electron gas (2DEG) create a large 2DEG concentration with high electron mobility, allowing high-voltage operation [1] [20]. Even though SiC materials are more commonly used in high-voltage due to low cost and commercial availability, GaN theoretically offers higher performances in high-power and high-switching frequency applications. However, the industrial interest and attention to GaN devices has seemingly increased steadily in recent years [18]. That allows GaN

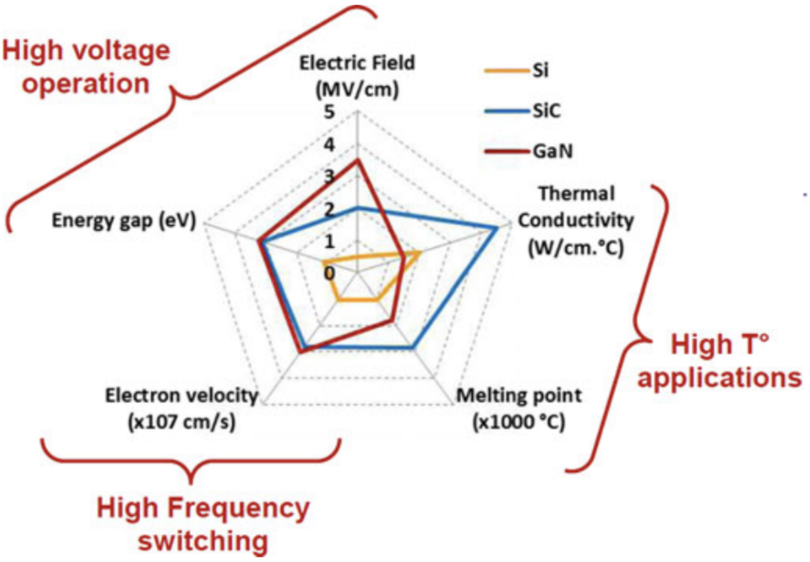

Figure 2.3: Summary of Si, SiC, and GaN relevant material properties.

devices to offer higher efficiency, lower switching losses, and increased power density compared to traditional silicon-based devices. Therefore, this research suggests using GaN semiconductors to employ eGaN FET devices.

To design the optimal Class Φ_2 inverter with GaN FETs, which can achieve ZVS conditions for reducing switching losses, components in the Class Φ_2 are selected based on specifications and applications, such as R_L, V_i, and P_{out}. Firstly, initializing sizing of Z_{MR} is approached by tuning the network components to peak at the fundamental and third harmonics while ensuring a zero impedance at the second harmonic. The components in Z_{MR} consists of the inductance of L_F, L_{MR}, and capacitance of C_{MR}, obtained by Eq. (2.1), Eq. (2.2), and Eq. (2.3) based on a selected capacitor C_F:

$$L_F = \frac{1}{9\pi^2 {f_s}^2 C_F} \tag{2.1}$$

$$L_{MR} = \frac{1}{15\pi^2 {f_s}^2 C_F} \tag{2.2}$$

$$C_{MR} = \frac{15}{16} C_F \tag{2.3}$$

The selection of the C_F provides a tradeoff between resonant losses and output power delivery, impacting efficiency. This is because a larger C_F value can reduce the network's impedance magnitude, which might be needed when the load impedance (Z_L) heavily burdens the drain impedance (Z_{DS}). Nevertheless, a smaller C_F value increases the impedance of the Z_{MR} components and decreases circulating currents. From this correspondence, calculation on the impedance Z_{MR} can be done by Eq. (2.4) with 65 pF of output capacitance (C_{OSS}) based on the drain-to-source voltage (V_{DS}) in switching device characteristics (GS66508T) referred to Fig. 2.4 [4].

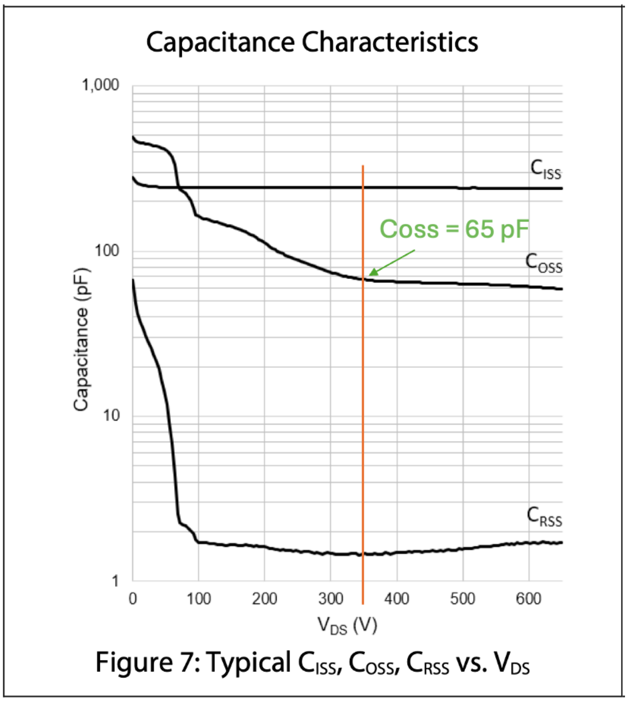

Figure 2.4: Characteristics of output capacitance in GS66508T [4].

$$Z_{\mathrm{MR}}(w) = wL_F // \left(jwL_{\mathrm{MR}} + \frac{1}{jwC_{\mathrm{MR}}} \right) // \frac{1}{jw(C_{\mathrm{OSS}} + C_P)} \tag{2.4}$$

In this research, a 4-nF series capacitance (C_s) is selected for filtering DC components in a load impedance, as shown in Fig. 2.2 [2, 3]. Since the C_s is sufficiently designed to be a large value, the DC voltage is blocked, allowing the neglect of C_s during the tuning process. Another component in the load impedance is a series inductance (L_S), which can be determined by the equation (2.5) based on load resistance (R_L) and power rating of the system.

$$L_S = \frac{1}{\omega}\sqrt{R_L\Big(\frac{8V_i^2}{\pi^2 P_{out}}\Big) - R_L} \tag{2.5}$$

After obtaining C_S and L_S, impedance in parallel with switching device Z_{DS}, which indicates the drain-to-source impedance losses, can be derived with Z_{MR} and Z_L by Eq. (2.7).

$$Z_L(w) = jwL_S + \frac{1}{jwC_S} + R_L \tag{2.6}$$

$$Z_{DS}(w) = Z_{MR}//Z_L \tag{2.7}$$

Z_{DS} and Z_{MR} are used for tuning L_S and C_F to achieve ZVS cooperation with lower peak switching losses. The optimal component values can be decided by tuning the magnitude and phase of Z_{DS} and Z_{MR} at fundamental, second harmonics, and third harmonics frequencies. At fundamental frequency, the phase angle of Z_{DS} is required to be within 30 and 60 degrees following the Eq. (2.8). Moreover, impedance Z_{MR} is supposed to be zero at the second-harmonic frequency as shown in Eq. (2.9).

$$30^\circ < \angle Z_{DS}(\omega_{sw}) < 60^\circ \tag{2.8}$$

$$Z_{MR}(2\omega_{sw}) = j2\omega_{2sw}L_{MR} + \frac{1}{j2\omega_{2sw}C_{MR}} = 0 \tag{2.9}$$

Besides, the difference between the magnitude of Z_{DS} at the fundamental and third harmonic frequency is supposed to be between 4 to 8 dB as shown in Eq. (2.10), and the inverter is more likely to operate at ZVS condition when the phase of Z_{DS} is below -80 degrees as shown in Eq. (2.11) [2] [3].

$$4 < |Z_{\text{DS}}(w_{\text{sw}})| - |Z_{\text{DS}}(3w_{\text{sw}})| < 8 \text{ dB} \tag{2.10}$$

$$\angle Z_{\text{DS}}(3w_{\text{sw}}) < -80^\circ \tag{2.11}$$

2.2 High-frequency Double-Layer Spiral Coil Design

Among many WPT coil structures, a circular coil is one of the most common coils in the WPT system. Still, this traditional design requires external capacitors as series compensators, leading to high voltage stress. Generally, a self-resonant (SR) coil is used for high-frequency applications. It provides a higher quality factor due to its higher inductance and lower resistance from internal capacitance, reducing losses from skin effect issues in traditional coils. Therefore, a self-resonant spiral coil structure is proposed in [6] and [7]. This structure, made from copper sheets instead of copper conductors as in traditional circular coils, is considered because of its parasitic capacitance between the pitch of the coil. This minimizes the losses due to the skin effect. The SR coils can also be classified into three structures: adjacent-turns coil, paralleled-layer structure, and parallel-plate-shaped coils structure, as shown in Fig. 2.5 [8]. [7] suggested that combining adjacent-turns coil, paralleled-layer structure into the multi-turn double-layer structure allows adding series capacitance C_s between adjacent turns and two conductor layers, which induces a resonant electric field. Consequently, increasing coil inductance leads to performing in a high-quality factor. Therefore, this research focuses on paralleled two-layer coils of SR spiral structure with adjacent turns, which have parasitic capacitance from both the gap distance between two layers and the pitch of each coil.

To design spiral SR coils, geometric specifications are the main indicators for

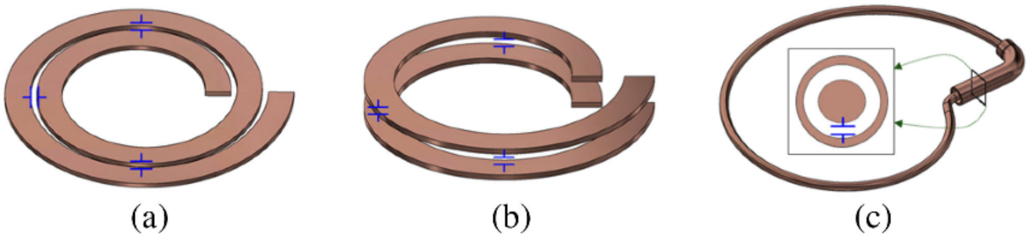
(a) (b) (c)

Figure 2.5: Classification of SR Coil (a) Adjacent turns; (b) Parallel plates; and (c) Coaxial capacitance on turns. [8]

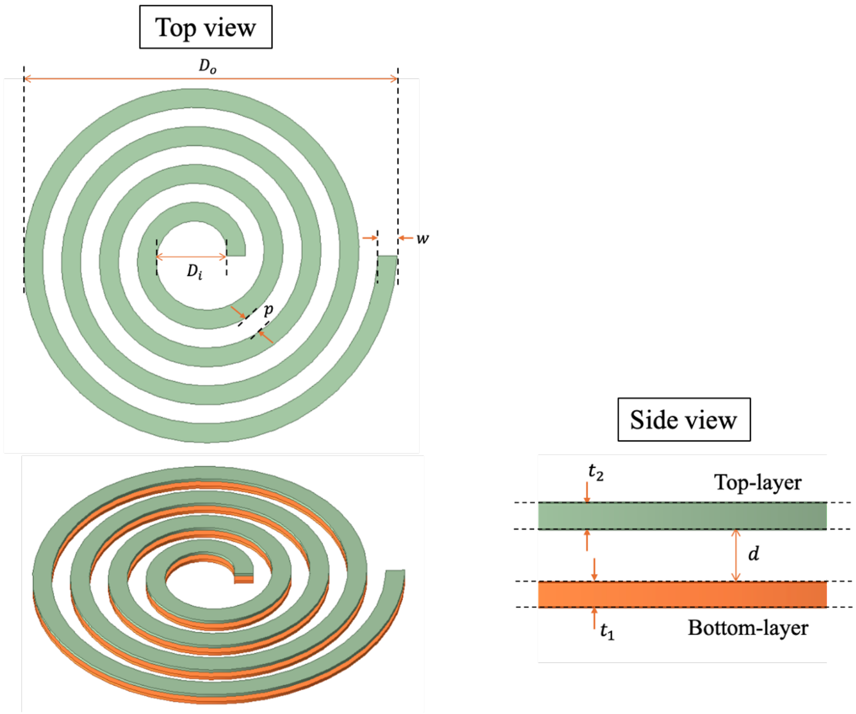

Figure 2.6: Uniform two-layer spiral coil structure.

Table 2.1: Design parameters for coil simulation.

Description	**Design Parameters**	**Unit**
Switching frequency	F_{sw}	MHz
Number of Turns	N	-
Outer diameter of bottom-layer coil	D_{o1}	cm
Outer diameter of top-layer coil	D_{o2}	cm
Inner diameter of bottom-layer coil	D_{i1}	cm
Inner diameter of top-layer coil	D_{i2}	cm
Distance between the layers	d	mm
Width of bottom-layer coil	w_1	mm
Width of top-layer coil	w_2	mm
Pitch of bottom-layer coil	p_1	mm
Pitch of top-layer coil	p_2	mm
Thickness of bottom-layer coil	t_1	mm
Thickness of top-layer coil	t_2	mm

quality factor values which are described in Table 2.1, such as outer coil diameter (D_o), inner coil diameter (D_i), the width of the coil (w), the thickness of the coil (t), the thickness of the dielectric layer (d), and the number of turns (N). The proposed spiral coils are designed in Archimedean spiral coil structure as shown in Fig. 2.6. The spiral coil is designed by using the polar coordinate system to determine the inner radius of the spiral structure from the desired outer diameter, including coil width and number of turns, as shown below:

$$R_i = \frac{D_o}{2} - \frac{3(w+p)N}{4} - w. \tag{2.12}$$

The inner diameter is derived by multiplying two times the inner radius and adding the polar to draw the spiral line in the polar coordinate system:

$$D_i = 2R_i + a\pi \tag{2.13}$$

where $a = \frac{w+p}{2\pi}$. Therefore, the adjacent-turn gap between its spiral coil called the pitch of the coil (p), is derived from substituting Eq. (2.12) and (2.13), which has a relationship of D_o, D_i, w and N, as shown below:

$$p = \frac{2\pi\left(D_o - D_i - \left(\frac{3\pi N + 4\pi - 1}{2\pi}\right) w\right)}{3\pi N - 1}. \tag{2.14}$$

Also, switching frequency (F_{sw}) is one of the essential parameters of quality factor generation. These parameters are related to the coils' inductance, capacitance, and resistance.

According to [7], the inductance is calculated by the equation (2.15), where μ is $1.2566 \times 10^{-6} H/m$ of magnetic permeability of copper, as shown below:

$$L_{coil} = \frac{\mu N^2 (D_o + D_i)}{4} \ln\left(\frac{2.46(D_o + D_i)}{D_o - D_i} + 0.2\left(\frac{D_o - D_i}{D_o + D_i}\right)^2\right) \tag{2.15}$$

Also, the capacitance of the coil is derived by Eq. (2.16) where ϵ is relative permittivity based on the material of the coil, in this study, applied $8.854 \times 10^{-12} F/m$ of copper relative permittivity and ϵ_0 is the air dielectric constant which is 1.0006 [7]:

$$C_{coil} = \frac{\epsilon\epsilon_0 \pi w N (D_o + D_i)}{2d}\left[1 + \frac{d}{\pi w}\ln\frac{2d}{\pi w} + \frac{d}{\pi w}\ln\left(1 + \frac{2d}{\pi w} + 2\sqrt{\frac{t}{d} + \left(\frac{t}{d}\right)^2}\right)\right]. \tag{2.16}$$

In addition, skin depth δ at switching frequency F_{sw} represents the conduction of the current density toward the surface of the coil as it is shown in Eq.(2.17) where ρ is the resistivity of the coil depending on the material of the coil. In this research, the coil is made from copper material with 1.68×10^{-8} Ω.m of the resistivity [7].

$$\delta = \sqrt{\frac{\rho}{\pi \mu F_{sw}}} \tag{2.17}$$

The total resistance consists of copper loss and dielectric loss. Dielectric loss R_c is gained from the equivalent coil capacitance by using this equation:

$$R_c = \frac{D_k}{2\pi F_{sw} C_{coil}}, \tag{2.18}$$

where D_k is a loss tangent. However, dielectric loss is assumed to neglect the loss tangent D_k because it is based on the dielectric material (air), which accounted for approximately zero in this research. Also, the copper loss is modeled as a combination of low-frequency loss caused by DC resistance and additional high-frequency loss due to eddy currents in the conductors. Therefore, the coil resistance is [7]:

$$R_{coil} = \frac{\rho \pi n (D_o + D_i)}{2w} \left(\frac{2}{\delta (1 - e^{1-\frac{t}{\delta}})} - \frac{4}{3t} \right) + R_c. \tag{2.19}$$

Maximizing coil inductance offers the optimal design of spiral coil; on the other hand, the resistance of the coil should be minimized as a relationship of quality factor:

$$Q = \frac{\omega L_{coil}}{R_{coil}}. \tag{2.20}$$

In uniform copper width two-layer SR coil [8], the self-resonant capacitance of the coil can be increased. Consequently, coil inductance increases the width of the coil or the number of turns in the uniform-width coil.

2.3 Motivation for Machine Learning-Based Coil Design

For high-frequency coil design, one of the challenges is to derive equations of related inductance and capacitance. Because of loss effects, including proximity effects and other undiscovered loss factors, it is also challenging to calculate the resistance. Therefore, a multi-physics simulator is essential to design the high-frequency coil. However, the advanced machine learning techniques in deep learning and neural networks in this study not only provide more accurate predictions but also significantly reduce the time required for simulations compared to conventional tools such as ANSYS software. Traditional simulation methods like ANSYS are often computationally intensive and time-consuming, taking approximately 3-5 minutes per simulation. Moreover, calculating the quality factor (Q) using conventional methods requires finding both the inductance and capacitance of the coil, which is a complicated process involving multiple iterative steps to find the optimal coil design.

In contrast, machine learning models can efficiently explore the design parameters, identify patterns, and predict optimal coil configurations with high precision. By reducing simulation times from minutes to potentially seconds, machine learning facilitates the development of coils with maximized quality factors and minimized resistance, which are crucial for efficient high-frequency WPT systems. This capability speeds up the design process and ensures that the resulting coil designs are highly efficient and effective for high-frequency applications. According to [10], the machine learning-based method is adopted in coil design optimization in high-frequency WPT applications. Furthermore, [21] applied a machine learning-based regression model and Non-dominated Sorting Genetic Algorithm II (NSGA-II) to find the optimal ferrite-structure coil design in a kilo-hertz frequency range for a high-power WPT system. Also, [22] offered artificial neural networks to optimize coil design for multi-objective coil dimensions for dynamic inductive power transfer systems. By employing machine learning, researchers can overcome the limitations of traditional simulation methods, leading to more innovative and high-performing WPT coil designs. However, the complexity of the proposed coil design increases compared to the other studies due to the large number of design inputs. This increases time consumption when optimizing Q and coil designs. Therefore, this study develops machine learning and mixed integer nonlinear programming algorithms to solve optimization problems with size and design constraints in application requirements, offering solving time reduction.

Chapter 3

Machine Learning-Based Quality Factor Estimation of the High-frequency Coil Design

Applying machine learning, especially neural networks (NN), enables learning and estimating desired outputs from provided inputs through network architectures as models for classification and regression problems. According to [10] and [21], it is recommended to apply deep learning and artificial neural networks, which are helpful for regression prediction purposes. For the optimization of coil designs, we can apply machine learning to quality factor estimation by predicting values of quality factors, which is our goal for coil design optimization from the trained model. This chapter will describe deep learning techniques and how training data is collected to design high-frequency coils in section 3.1 and section 3.2. Also, we will discuss deep learning model training strategies in section 3.3, including model evaluation and selected models in section 3.4.

3.1 Deep Learning Technique for High-frequency Coil Designs

Deep learning is a subsection of machine learning with multiple layers of hidden neurons, known as artificial neural networks, allowing the network to learn complex tasks and process large amounts of data, for example, image recognition, information-processing prediction, and regression problems. Each layer in the network processes the input data, called input neurons, and passes it on to the next layer, gradually extracting more abstract features [23]. The regression aims to predict a continuous output value based on input data by adopting supervised machine learning with neural network architecture. Also, this study focuses on estimating quality factors from 13 input neurons based on geometric coil design parameters as represented in Table 2.1 with deep learning technique.

The basic concept of a neural network model is to take an input, x, along with a bias, b, and multiply them by weights, ω. These weighted inputs are then summed together. The bias is a single value, while the input and weights are vectors, $x \in \Re^n$, and $\omega \in \Re^n$ with their dimensions, n, determined by the size of the input, as shown in Fig. 3.1. The input data is passed through the hidden layers, where each neuron performs a weighted sum of the inputs and applies an activation function ϕ to produce an output as shown below:

$$z = \omega^T x + b = \omega_1 x_1 + \omega_2 x_2 + .. + \omega_n x_n + b, \tag{3.1}$$

$$y = \phi(z). \tag{3.2}$$

The activation function, also known as a unit function or transfer function, performs a nonlinear transformation of z such as ReLu, Sigmoid, Hyperbolic tangent, Softmax, etc. The Rectified Linear Unit (ReLU) is an activation function that has gained popularity in deep learning due to its fast learning speed and superior performance compared to other activation functions like Sigmoid and Hyperbolic tangent [24].

The ReLU function is nearly linear, which means it retains the properties of linear models that make them easy to optimize using gradient-descent methods. The ReLU function applies a threshold operation to each input element, setting values less than zero to zero considering the max of the function:

$$y = ReLU(z) = max(0, z) = \begin{cases} 0, & \text{for } z < 0. \\ z, & \text{for } z \geq 0. \end{cases} \tag{3.3}$$

This allows the ReLU to effectively capture nonlinear patterns in the data while maintaining the simplicity and efficiency of linear models [24]. Eventually, the outputs, y, from the last hidden layer are passed through the output layer, producing the final regression prediction.

Moreover, neural networks can be classified into different structures, such as Feedforward Networks (FNNs), Recurrent Neural Networks (RNNs), Convolutional Neural Networks (CNNs), etc., based on passing data techniques and arrangement of the neurons [23]. The most straightforward architecture of a neural network is a feedforward structure. The inputs proceed to the output of the neurons with no feedback from the outputs throughout the network. The feedforward neural net-

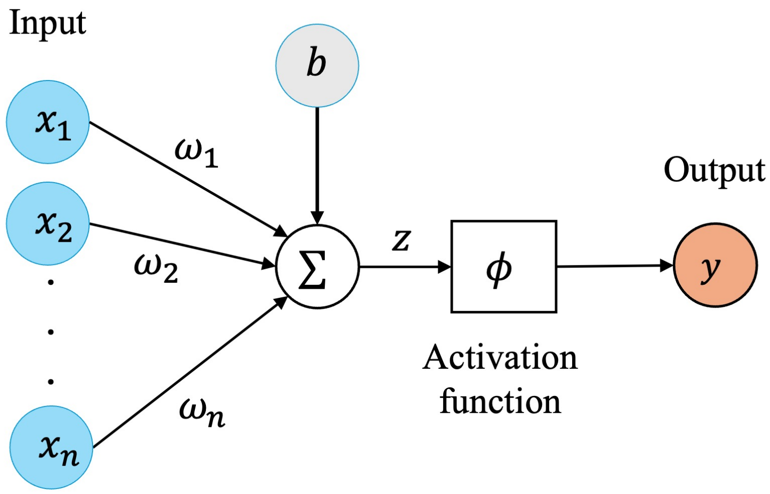

Figure 3.1: Basic neural network architecture.

works are classified into single-layer and multilayer. The multilayers of the network, also called deep feedforward neural network (D-FFNN), are categorized into one hidden layer and multiple hidden layers, intervening between the input and output layer. In contrast, the single-layer feedforward neural network is directly passed on to the output layer. The input layers pass on weight and bias and compute the output results in a single-layer structure, as shown in Fig. 3.1.

This research employs a deep feedforward neural network architecture with two hidden layers trained with Python using the Keras library of the TensorFlow package, open-source software, and a highly productive interface, focusing on modern deep learning and solving machine learning problems. Keras offers benefits such as concise code, fast machine-learning workflow, and deployment of hyper-parameter tuning. In the case of high-frequency double-layer spiral coil designs, supervised learning of quality factor is a target of the D-FFNN model with 13 input design features learned through two neural network hidden layers, as shown in Fig. 3.2.

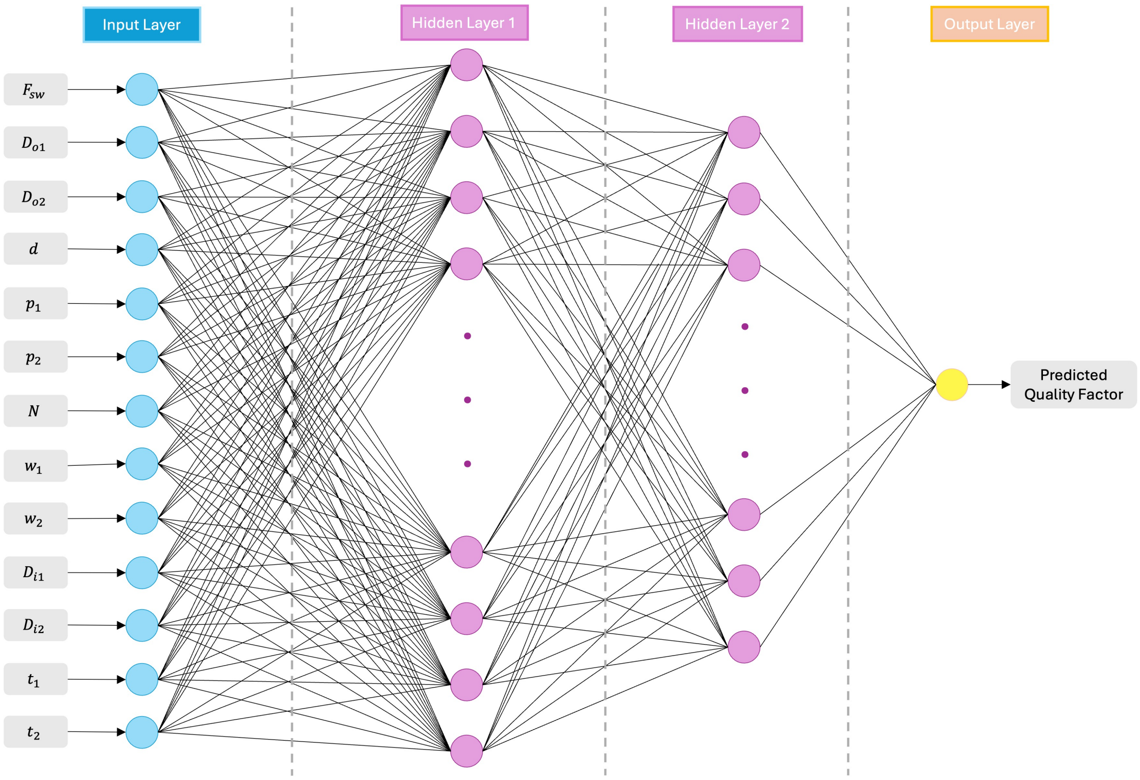

Figure 3.2: A Deep Feedforward Neural Network (D-FFNN) with 13 input neurons, two hidden layers, and one output.

Since the D-FFNN model is generated, the next step is to evaluate its performance and whether it optimally fits the supervised Q factor via model performance estimation metrics called loss functions. The loss functions are evaluation tools that indicate the mismatch between the predicted and given output values in statistical measurement. The typical examples of model evaluation metrics are Mean Square Error, Mean Absolute Percentage Error, and a coefficient of determination (R-square or R^2). Each loss function has characteristics that indicate the performance of different applications. Generally, Mean Squared Error (MSE) is commonly applied for regression problems as a loss function because it identifies outliers and imbalances in the dataset by calculating the average of the squared differences between predicted ($\hat{y}_i$) and actual (y_i) values as shown in Eq. (3.4):

$$\text{MSE} = \frac{1}{n}\sum_{i=1}^{n}(\hat{y}_i - y_i)^2. \tag{3.4}$$

Therefore, the small values of MSE represent how well the performed model does due to the sensitivity of large errors and outliers. Similarly, the small values of Mean Absolute Percentage Error (MAPE) express the small relative error in a different scale as a percentage, as shown in Eq. 3.5. It is suitable for non-closely zero or non-infinity actual values, leading to undefined or exaggerated percentage errors.

$$\text{MAPE} = \frac{100\%}{n}\sum_{i=1}^{n}\left|\frac{\hat{y}_i - y_i}{y_i}\right| \tag{3.5}$$

On the other hand, the R^2 loss function measures the proportion of variance in the dependent variable that is predictable from the independent variables offering an indication of the goodness of fit where $\overline{y}$ is the mean of the actual values.

$$R^2 = 1 - \frac{\sum_{i=1}^{n}(\hat{y}_i - y_i)^2}{\sum_{i=1}^{n}(y_i - \overline{y})^2} \tag{3.6}$$

The next chapter will continue applying the model to maximize quality factors for achieving the most optimized coil design in high-frequency WPT systems.

3.2 Data Collection for the High-frequency Coil Designs

Input features can approach model training for quality factor estimation to supervise the D-FFNN model in a hidden-layer neural network for deep learning from the supervised quality factor output gathered in the previous coil simulation. Table 3.1 represents various data collections of double-layer spiral coil designs based on 13 coil design parameters, for example, switching frequency, number of turns, the width of the coil, the thickness of the coil, etc. They are gathered by implementing parametric mode in ANSYS simulation to find the quality factor as the model's output. The simulations assume the same outer diameter size of D_{o1} and D_{o2} and the same thickness of t_1 and t_2. The valid designs have collected 27,720 cases from 55,296 designs for training the model in this study. This is because it is impossible in some double-layer spiral coil structure cases. However, the collected data are considered large numbers and enough to train the model and evaluate the performance of the model corresponding to [9, 10].

Table 3.1: Data collection for the training model.

Variables	**Values**	**Number of splits**
F_{sw}	6.78, 13.56, 20.34, 27.12 MHz	4
N	3, 4, 5, 6	4
d	2, 4, 6 mm	3
D_{o1}, D_{o2}	100, 120, 140, 160 mm	4
t_1, t_2	0.5, 1.0 mm	2
w_1	6, 8 10, 12 mm	4
w_2	6, 8 10, 12 mm	4
p_1	4, 6, 8 mm	3
p_2	4, 6, 8 mm	3
D_{o1}	6, 7, 8, ..., 108 mm	-
D_{o2}	6, 7, 8, ..., 108 mm	-
Total (4x2x4x4x3x4x4x3x3) = 55,296 cases (27,720 valid cases)		

By collecting data in ANSYS software, it is computationally expensive to simulate quality factors in terms of time consumption, resources, and processing. Furthermore, the simulations result in equivalent coil impedance (Z-parameter), which is required to extract resistance and reactance to calculate the quality factor from the equation (2.20) in Chapter 2. After the data collection, the data are saved in a CSV file and ready to continue training the model, considering training strategies to achieve the best performance of the model.

3.3 Deep Learning Model Training Methodology

Several strategies are employed to achieve the most effective D-FFNN model during training. Proper weight initialization, such as Xavier or He initialization, assists in achieving faster convergence and avoids vanishing gradient issues. Also, the Adam optimizer, also called Adaptive Moment Estimation, is used to update the network weights iterative and minimize the loss function as a stochastic gradient descent algorithm to optimize the learning process. Moreover, K-fold cross-validation helps to monitor performance on validation sets to ensure the model performs well across different data subsets. These strategies collectively make the training process of the D-FFNN model more efficient, leading to a robust and high-performing neural network. In this study, we chose these methods to train and improve the D-FNN model, the details of which are described in the following sections.

By using deep learning models with multiple hidden layers, the network can learn complex relationships between the input features and the target output, allowing for more accurate regression predictions. To develop the model's accuracy, it is recommended to adopt model training strategies, such as weight initialization, k-fold cross-validation technique, hyper-parameter tuning, and training data splitting. These techniques maximize the model's performance, which will be discussed further in this chapter.

3.3.1 Weight Initialization

Generally, implementing only ReLU activation functions is claimed to experience dying ReLU issues, which cause an output of zero for any input. This phenomenon is called the vanishing gradient from inactive ReLU neurons [26]. One of their merits is that ReLU activation functions result in the same value for every data passing, leading to less accurate model performance. Consequently, it is difficult for the neural network to learn since the neurons take a wide range of values. To prevent extremely deep and narrow over-fitting with the ReLU function in D-FFNNs, weight, and bias initialization are suggested to restrain the dying ReLU problem [25]. Initializing the weights and biases worked with the activation function is essential to minimize the loss function and shorten convergence time. In this research, Xavier initialization, another name for Glorot initialization, is adopted to adjust the variance of the initial weights to prevent the gradient exploding problem, allowing stable training dynamics for both forward and back-propagation. It scales the weights by setting the standard deviation based on the number of inputs and outputs applied to each layer. Moreover, it is implemented along with Adam optimizer, enabling it to minimize the cost function as a stochastic gradient descent algorithm according to [10, 25].

3.3.2 Training, Validation, and Testing Dataset

Training D-FFNN models start by dividing datasets into training and testing datasets for different purposes. The training dataset is implemented for the training model. Since this part is the most important for supervised model learning, the proportion of this dataset is supposed to be input into a large amount of overall datasets. However, an excessive number of training data inputs causes the over-fitting problems of the model [28]. The optimized proportion is supposed to be considered based on the characteristics of the data and model performance. Also, model performance evaluation is required to explore how it fits via model evaluation metrics with the testing dataset.

The training sets are subjected to a model training process, and testing datasets are used as evaluation tools. However, the model can indirectly influence over-fitting. Also, it is suggested that available data be split into three partitions: training, validation, and testing datasets. The validation datasets help tune model hyper-parameters, leading to maximizing model performance. This idea is suitable for large data samples inputting in the model due to potential sampling bias [27]. There are various validation methods during training, such as the K-fold cross-validation method. Due to its less biased capability, it is recommended that it be implemented to optimize model-tuning variables. This allows the model to obtain the best results along with hyper-parameter tuning, which will be discussed in the following subsection.

3.3.3 K-fold Cross Validation and Hyper-parameter Tuning

To improve predictive capabilities, optimization of neural network variables assists in exploring the possibility of obtaining more accurate outputs through tuning strategy. In this study, hyper-parameter tuning and the K-fold cross-validation technique are applied to develop the model's performance. Proper tuning can find the balance between model complexity and simplicity, causing significant error reduction in predicted outputs. Hyper-parameter tuning prevents over-fitting and under-fitting scenarios and ensures the model performs well on unseen data. Combining this technique with K-fold cross-validation is suggested, which helps to train and validate the performance by dividing training datasets into k folds. The divided datasets are fitted and validated in each fold, combined with hyper-parameters exploration such as parameter grid search and random search algorithm [28]. For each combination, the configuration is selected from k-fold cross-validation and the most accurate average of performance based on the chosen evaluation metric as shown in Fig. 3.3. Effective hyperparameter tuning can lead to more efficient use of computational resources, reducing training time and costs while achieving better results, making it essential for practical applications in machine learning.

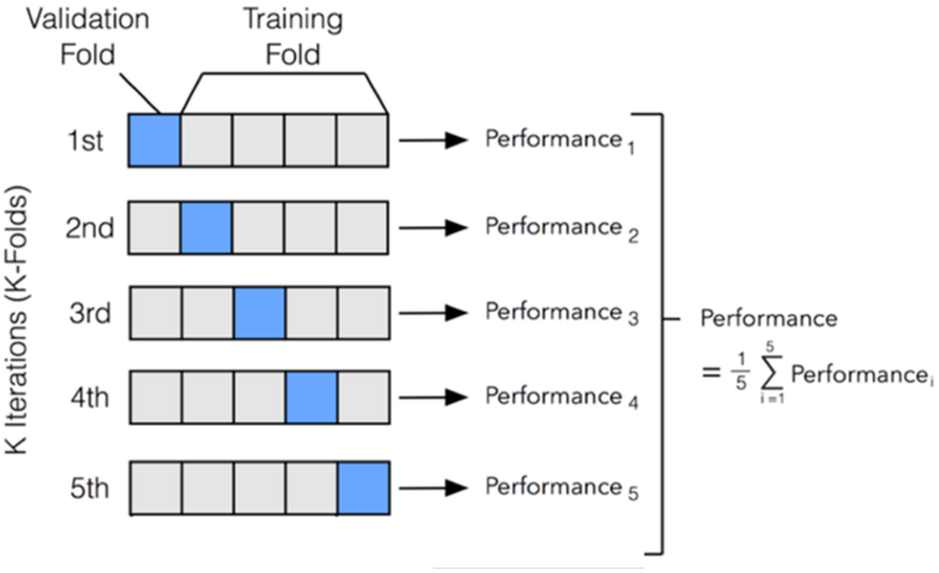

Figure 3.3: K-fold Cross-validation diagram with five folds.

3.4 Model Training and Performance Evaluation

In this research, the D-FFNN model is implemented for estimating the Q factor of the spiral coil using the datasets formed in Table 3.1 showing 13 input features. The model contains two hidden layers with 64 and 32 neurons in each layer, respectively. Moreover, the ReLU activation function is applied between each layer, including the initialization of weight and bias. In addition, the training model is applied to the Adam optimizer to improve the learning process. The ML-based quality factor estimation section in the upper green dash section in Fig. 4.2 represents the workflow of quality factor estimation from ANSYS simulation and D-FFNN model. Their Q-factor outputs are used to evaluate the model performance.

Before tuning the hyper-parameter called the pre-trained model in the first training model, the model is implemented 90% of the training dataset, 10% of the validation dataset, and 10% of the testing dataset. In addition, the learning rate is assumed to be 0.01, and the batch size of each training epoch is set to be 64 over 500 epochs in the pre-trained model. Fig. 3.4 represents the MSE loss during the 500-epoch training and validation process. As you can see, the loss behavior scatters in the validating process, denoted as red stars in the plot. While the values of

MSE significantly dropped from the beginning of the training and then remained stable around 1800 of training data input between 200 epochs and 500 epochs, the pre-trained model is mostly validated around 1600 of MSE, approximately, which is a lower value than the training. This describes that model training ability is not fitted efficiently with the validation sets, consequently leading to possibly predicting inaccurate quality factors with high MSE of testing results.

To improve the performance of the model, it is crucial to explore different performance models with mentioned training strategies. In this study, five sets of dataset splits are experimented into 90%/10%, 80%/20%, 70%/30%, 60%/40%, and 50%/50% of the training/testing dataset. This allows us to select the optimal model in terms of model performance. Table 3.2 shows the model performance evaluation values from different data split proportions. The performances are observed with MSE, MAPE, and R^2. The most common metric is the mean square error represented by the errors between the predicted and actual Q-factors from the simulation. As you can see in Table 3.2, the predicted outputs of Model 3 are less fitted with the simulated Q-factor perceiving from the most significant number of the MSE,

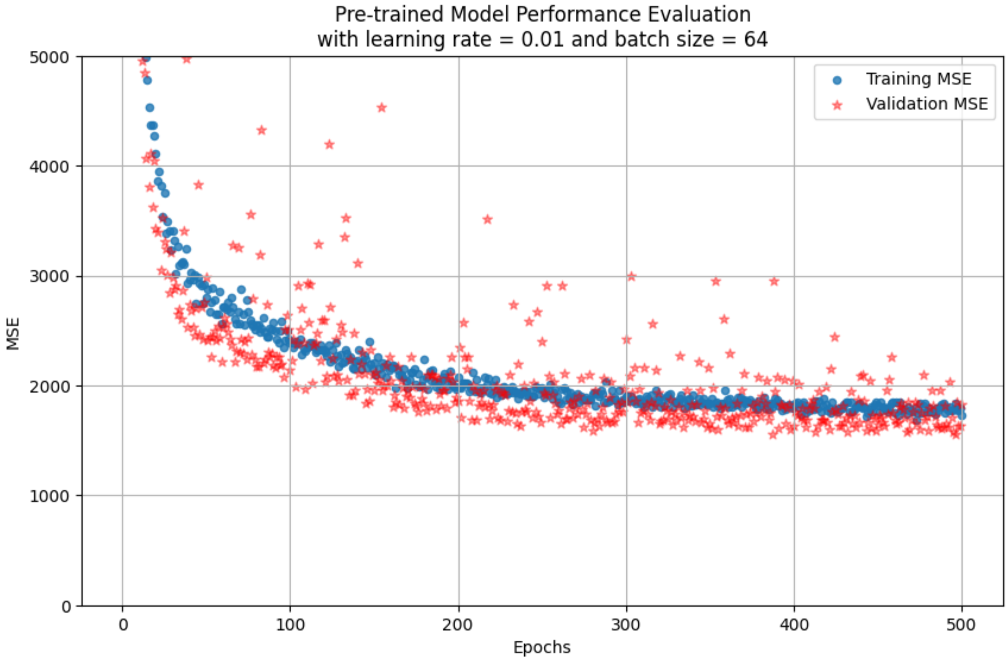

Figure 3.4: A pre-trained model with 64 batch size and 0.01 learning rate over 500 epochs.

Table 3.2: Quality Factor Evaluation from Different Testing Datasets.

Model Name	%Training/%Testing datasets	MSE	MAPE	R^2
Model 1	90%/10%	1314.2813	3.6461%	0.9784
Model 2	80%/20%	1404.6434	3.5731%	0.9778
Model 3	70%/30%	1632.0887	4.1571%	0.9742
Model 4	60%/40%	1465.7823	3.7332%	0.9768
Model 5	50%/50%	1547.4684	3.9712%	0.9756

MAPE, and the smallest R^2 value, whereas Model 1 performance can defeat all of the proportions which indicate good performance. Even though its MAPE value is observed to be the second lowest rank, Model 1 is evaluated with the highest R^2 accounting for 0.9784, meaning that the output is efficiently predicted from the independent inputs. Therefore, Model 1 is considered to be selected due to the most optimal performance among other data splits.

Moreover, the performance of selected models is noticeably improved from that of the pre-trained model. Integrating the techniques mentioned above into the neural network training process, MSE decreased from 1637.49 of the pre-trained model to 1314.28 of the post-tuning model, accounting for 21.02 % when evaluated with testing set as shown in Fig. 3.4 and 3.5, respectively.

Once the model is trained, it performs efficiently and can predict the most accurate quality factor. Then, the optimization of Q will be implemented by providing a range of features based on applications and specifications, as shown in the next chapter.

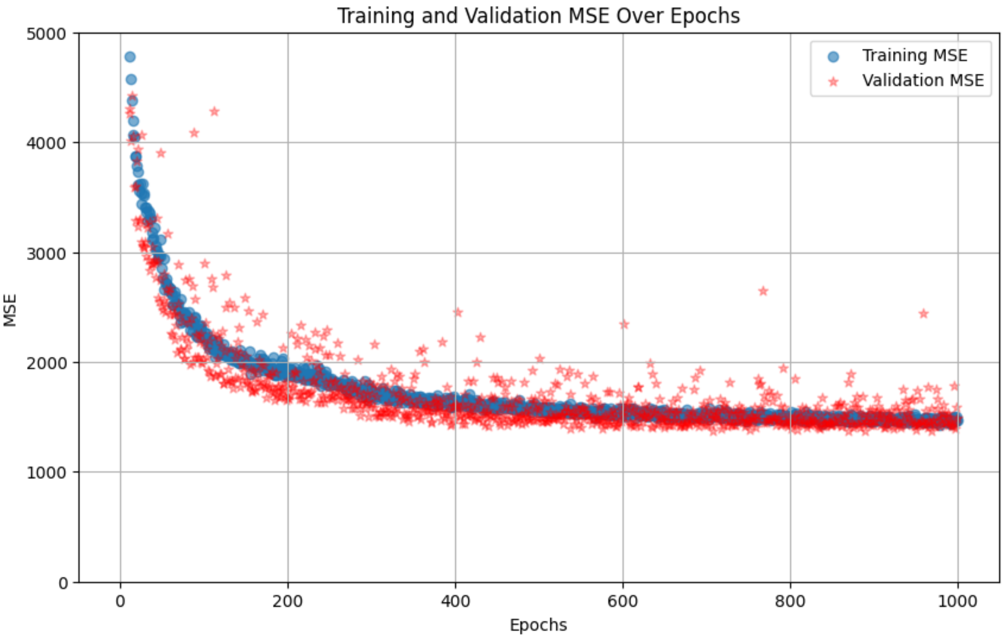

Figure 3.5: A post-trained model with 64 batch size and 0.001 learning rate over 1000 epochs.

Chapter 4

Optimization of the High-frequency Coil Design

Once the ML-based Q factor estimation model is satisfied in Chapter 3, the next target is to find an optimized design of a double-layer spiral coil for the WPT system. The idea of the optimization is to implement the accurate ML model to obtain the design parameters with a maximum quality factor. This chapter will explain the general optimization algorithms and the algorithm suitable for non-convex and mixed integer nonlinear programming (MINLP) problems, including the MINLP problem for the self-resonant coil optimization problem of this study.

4.1 Optimization Algorithms

The optimization algorithms are suggested as a tool to solve various optimization problems and also suggest coil designs and coil dimension setups restrained by design requirements and physical design limitations [29]. Fig. 4.1 demonstrates optimization algorithms based on exhaustive search, deterministic, and stochastic solving methods. Extensive search is considered a direct and simple method that explores possible designs. However, the number of search space sets can have large combinations based on the number of variables [29]. Some researchers proposed optimization of coil design with an exhaustive search algorithm by providing design space of design parameters and filtering the optimal cases to build a spiral coil, allowing to save computational cost [10]. Otherwise, [21] and [22] suggested genetic algorithm (GA) in multi-objective optimization of the coil dimensions design in high-frequency WPT systems and dynamic inductive power transfer (DIPT) systems, respectively. They claimed it is difficult to utilize an exhaustive grid search due to the large number of input parameters and system outputs. The genetic algorithm is one of the meta-heuristic stochastic algorithms, including particle swarm optimization (PSO). The natural selection process inspires GA in a real-life problem similar to feeding animals called particles of PSO. GA's algorithm starts searching by randomly selected and changed input combinations based on the initial population, crossover, and mutation [22]. Moreover, [29] claimed an excellent balance of the robustness and the computational cost with high-dimensional input samples. Nevertheless, their randomness and finding optimal acceptable parameters of the algorithm cause comprehensive tuning and have a slow convergence rate. In addition, loose constraints with only the boundaries of the parameters result in impossible cases due to a lack of the MINLP solving ability.

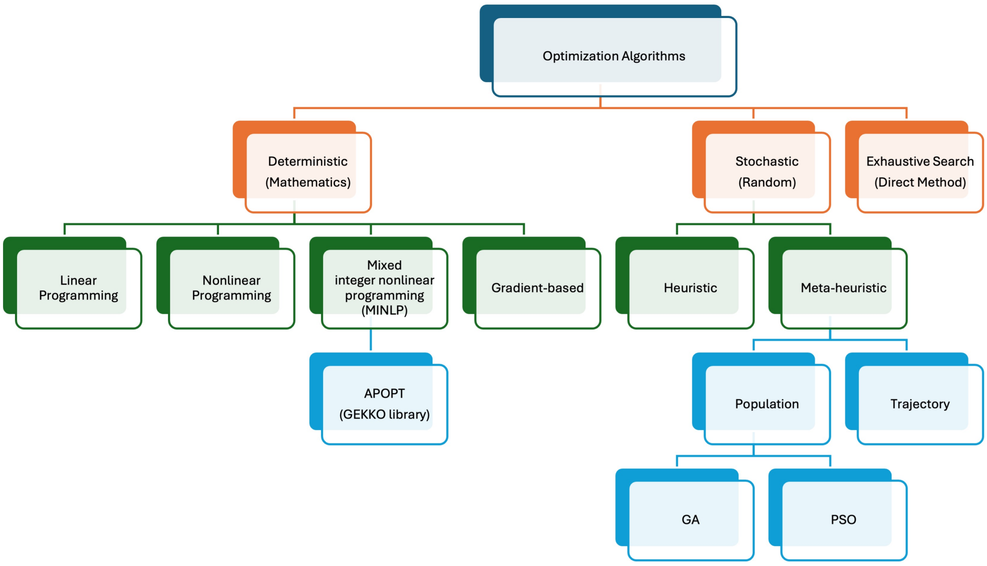

Figure 4.1: Optimization Algorithm Chart Diagram.

This study implements deterministic optimization to optimize the spiral coil design with a maximum quality factor. It has fast convergence properties for solving large-scale optimization problems, while the design space diversity is a downside of this method [29]. However, the Advanced Process Optimizer (APOPT) algorithm can solve MINLP problems and satisfy both inequality and equality constraints, including the whole number of coil turns. The Gekko package in Python provides a tool for single-objective and multi-objective problems. It covers operation mode of optimization, dynamic simulation, and control integrated with machine learning, enabling the solving of engineering problems [30]. Therefore, this library is suitable for this research's target, as you can further see the optimization results comparing simulation and ML-based quality factor estimation in the next section.

4.2 Proposed-Coil Optimization Problem with APOPT Solving Algorithm

Fig. 4.2 demonstrates a workflow diagram for integrating ML-based quality factor estimation and coil design optimization process. In the quality factor estimation, the design parameters serve as inputs to generate the Q-factor from both the ANSYS

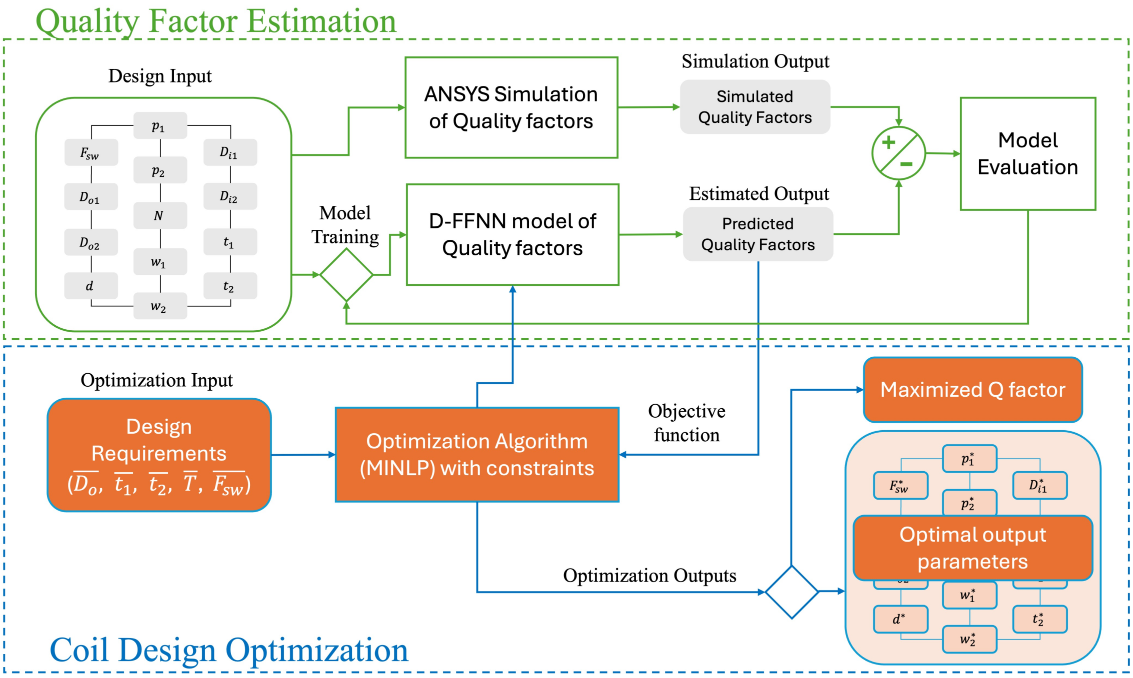

Figure 4.2: Block diagram for quality factor estimation and double-layer spiral coil design optimization.

simulation and the D-FFNN model. The results of Q-factors from the simulation in ANSYS software are used for training and evaluating the model to acquire the accurate model following Chapter 3. The model is applied as an objective function to optimize the designs to predict a Q-factor, which can find the optimal coil design with the maximum predicted Q-factor. The optimization process starts by providing design requirements based on coil outer diameter, copper coil thickness, and operating switching frequency into the optimization algorithm's input.

The optimization algorithm searches the optimal design parameters of the spiral coil configuration to maximize quality factors. In this study, the APOPT is proposed as the optimization algorithm to maximize quality factors due to its ability to solve large-scale optimization problems. The optimization problem for this research is represented in Eq. (4.1) with coil design constraints and search boundaries denoted that the number of coil turns is restricted to be a positive non-fractional real number:

$$\begin{aligned}
\max_{x\in V} \quad & Q_{pred}(F_{sw},\, D_{o1},\, D_{o2},\, d,\, p_1,\, p_2,\, N,\, w_1,\, w_2,\, D_{i1},\, D_{i2},\, t_1,\, t_2) \\
\text{subject to} \quad & F_{sw} = \overline{F_{sw}},\ D_{o1} = D_{o2} = \overline{D_o},\ D_{i1} = D_{i2} \\
& t_1 = \overline{t_1}, \quad t_2 = \overline{t_2} \\
& p_1 = \frac{2\pi\left(D_{o1} - D_{i1} - \left(\frac{3\pi N + 4\pi - 1}{2\pi}\right) w_1\right)}{3\pi N - 1} \\
& p_2 = \frac{2\pi\left(D_{o2} - D_{i2} - \left(\frac{3\pi N + 4\pi - 1}{2\pi}\right) w_2\right)}{3\pi N - 1} \\
& D_{i1} \le D_{o1}, \quad D_{i2} \le D_{o2} \\
& p_1 \le w_1, \quad p_2 \le w_2 \\
& t_1 + t_2 + d \le \overline{T}, \quad 2 \le d \le 5 \text{ mm} \\
& 5 \le D_{i1} \le 50 \text{ mm}, \quad 5 \le D_{i2} \le 50 \text{ mm} \\
& 5 \le w_1 \le 20 \text{ mm}, \quad 5 \le w_2 \le 20 \text{ mm} \\
& 1 \le p_1 \le 15 \text{ mm}, \quad 1 \le p_2 \le 15 \text{ mm} \\
& N \in \{2, 3, 4, 5, 6, 7, 8\}
\end{aligned} \tag{4.1}$$

To satisfy all constraints, the problem is considered a non-convex and a mixed integer nonlinear programming (MINLP) problem. Accordingly, the required coil design specifications are inputs of this problem as written in the form of $A \in \{\overline{D_o}, \overline{t_1}, \overline{t_2}, \overline{T}, \overline{F_{sw}}\}$ where ($\overline{D_o}$) denoted as overall outer diameter, $\overline{t_1}$ and $\overline{t_2}$) represented a thickness of copper coils of top-layer and bottom-layer. Also, the required coil thickness setup and desired switching frequency are denoted as ($\overline{T}$) and ($\overline{F_{sw}}$), respectively. The input of the problem is the 13 design parameters for Q estimation in the trained D-FFNN model, represented as $V \in \{F_{sw}, D_{o1}, D_{o2}, d, p_1, p_2, N, w_1, w_2, D_{i1}, D_{i2}, t_1, t_2\}$. Otherwise, the optimization outputs are two results: 1) the highest quality factor (Q^*_{pred}), and 2) the optimized design parameters that obtain the highest Q factor denoted as $V^* \in \{F^*_{sw}, D^*_{o1}, D^*_{o2}, d^*, p^*_1, p^*_2, N^*, w^*_1, w^*_2, D^*_{i1}, D^*_{i2}, t^*_1, t^*_2\}$.

To avoid invalid designs and limit the searching boundary, the values of design parameters are restrained in the different upper-bounds and lower-bounds in inequality constraints shown in Eq. (4.1). For example, the size of the coils is bounded between 5 mm and 50 mm of inner diameter and 5 mm and 20 mm in width for both layers. The distance between two layers is limited to be greater than 2 mm and less than 5 mm. In addition, adding equality constraints such as $p_1 = \frac{2\pi\left(D_{o1} - D_{i1} - \left(\frac{3\pi N + 4\pi - 1}{2\pi}\right) w_1\right)}{3\pi N - 1}$, and $p_2 = \frac{2\pi\left(D_{o2} - D_{i2} - \left(\frac{3\pi N + 4\pi - 1}{2\pi}\right) w_2\right)}{3\pi N - 1}$ can prevent impossible design cases. Meanwhile, the outer diameter, inner diameter, and thickness of the coils are assumed to be equal in size in this study. Also, the operating frequency is designed to be the same as the Class Φ_2 inverter operation. However, the number of coil turns is required to be a whole number, and then it is selected in a set of integer numbers between 2 and 8. The results of the coil optimization will be shown in Section 5.2, including its efficiency compared to simulation and an experimental prototype.

4.3 Observation on the Proposed Coil Optimization

To conclude this chapter, the APOPT algorithm solves double-layer spiral coil optimization problems. The quality estimation from the D-FFNN model provides input in the optimization algorithm and satisfies both constrained MINLP problems. The requirement of geometric design is supplied to limit searching space and save operating time, resulting in the highest Q. The Q factor is simulated and estimated to compare the performance of the proposed method and the simulation, as the details are shown in Section 5.2.3. The optimal result from the model provides the 963.27 highest Q with the design of a 2.37-mm air-layer distance of a 20-cm spiral coil. In contrast, the Q-factor of the coil prototype results in 551.31, which seems to be lower than the simulation, accounting for 45.21%. However, Experiment 2, with a 3.38-mm air-layer distance design, provides a higher Q, accounting for 777.53. It is observed that Experiment 1 can only achieve resonant frequency at 10.63 MHz, which is lower than the desired 13.56 MHz frequency.

To optimize the coil design in the desired resonant frequency, the optimization method must be developed by including resonant conditions, offering the optimal optimization outcome. The operation under the resonant frequency (f_0) occurs when specific capacitive reactance and inductive reactance are canceled out at the particular frequency as shown below:

$$f_0 = \frac{1}{2\pi\sqrt{L_{coil}C_{coil}}}. \tag{4.2}$$

Therefore, the resonant frequency is used to limit through the inductance's and capacitance's equation (2.15) and (2.16) in Chapter 2.2. It is bounded with the inequality equation with an acceptable range within a small error of the desired frequency, assuming within a 10% range as shown below:

$$F_{sw} - 10\%F_{sw} \leq \frac{1}{2\pi\sqrt{L_{coil}C_{coil}}} \leq F_{sw} + 10\%F_{sw}. \tag{4.3}$$

This constraint assists the optimization algorithm in satisfying both the resonant operation and the design constraints, offering the optimal Q-factor and other design parameters. However, in this study, the optimal results with new constraints are very challenging because of the strictly optimizing process on the resonant frequency operation. It is suggested that this optimization method be improved in further study.

Chapter 5

Experimental Results

5.1 13.56 MHz Frequency Class Φ_2 Inverter Design

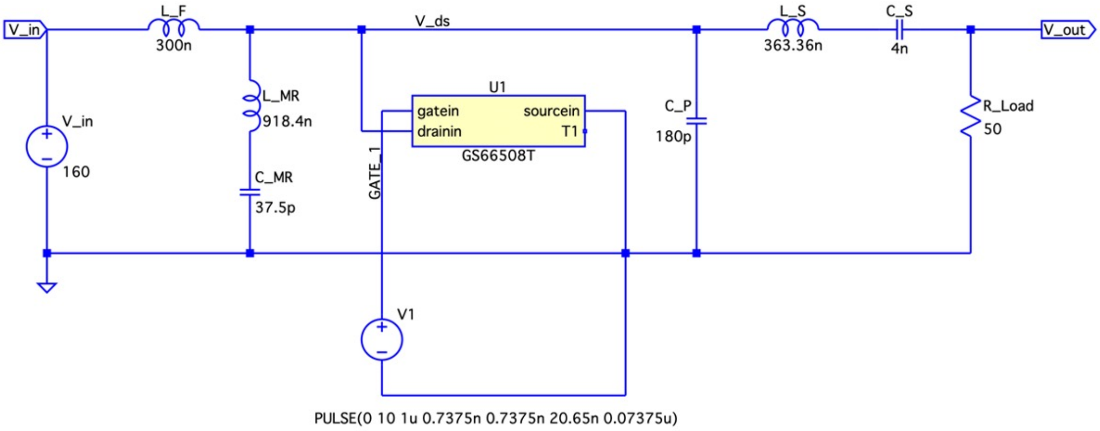

Figure 5.1: Circuit diagram of a 300-W Class 2 inverter with a 160 V DC input voltage, featuring a 300 nH L_F, a 918.4 nH L_{MR}, a 37.5 pF C_{MR}, and a 240 pF parallel capacitor, including a 65 pF C_{OSS} on the input side. It also includes a 363.36 nH L_S and a 4 nF C_S, designed to operate with a 50 Ω load using a GS66508T eGAN FET switching device in LTspice.

Class Φ_2 Inverter can be simulated in LTspice software for essential values, such as drain-to-source voltage, power output waveform, etc., in the circuit with LTspice software. The circuit diagram using the GS66508T switching device is shown in Fig. 5.1. The circuit component values, for example, L_{MR}, C_{MR}, and L_S, can be directly derived in the Eq. (2.2), Eq. (2.3), and Eq. (2.5) from Chapter 2.1. However, L_F and C_P are supposed to be properly tuned for performing in the ZVS condition suggested in the criteria, as shown in Eq. (2.8), Eq. (2.9), Eq. (2.10), and Eq. (2.11).

In the LTspice simulation, the value for the C_P component should be highlighted due to distinguishing characteristics of parasitic output capacitance (C_{OSS}) in GS66508T. Even though, for example, the calculation of C_P value is 240 pF, in simulation, C_P should be excluded from 65 pF of C_{OSS}, accounting for 180 pF.

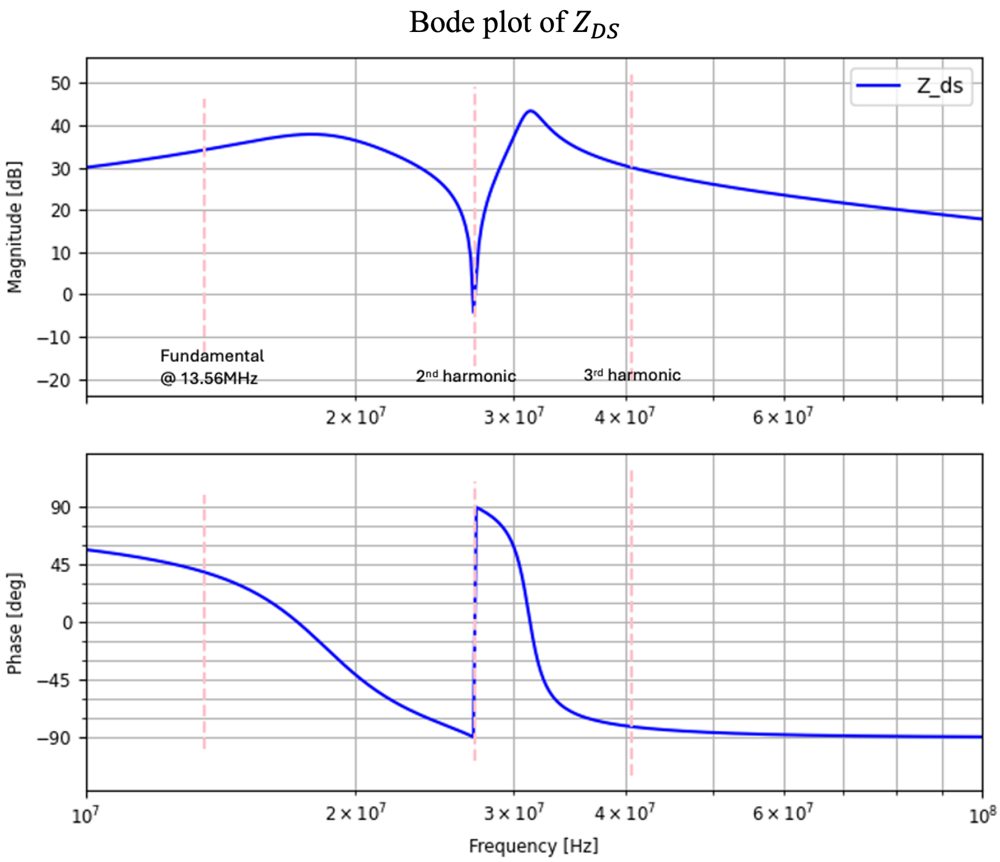

Figure 5.2: Bode plot of Z_{DS}.

Furthermore, the bode plot in Fig. 5.2 shows the magnitude and phase of Z_{DS} after the component value's tuning. At the fundamental frequency of 13.56 MHz, the phase of Z_{DS} is supposed to be within 30 and 60 degrees. Also, the magnitude of the difference between Z_{DS} at fundamental and third-harmonic frequency is suggested to be between 4 dB and 8 dB. Moreover, the phase angle at third-harmonic frequency is around -85 degrees, which is the recommendation for a phase angle lower than

Table 5.1: Class Φ_2 inverter performance in three fine-tuning experiments.

Parameters	**Case 1**	**Case 2**	**Case 3**
L_F	300 nH	260 nH	360 nH
C_P	240 pF	280 pF	200 pF
C_P (simulation)	180 pF	220 pF	140 pF
P_{out}	300.827 W	300.920 W	298.746 W
Maximum V_{DS}	345.373 V	342.888 V	347.139 V
% Efficiency	99.25%	98.99 %	99.05%
$\lvert Z_{\mathrm{DS}}(w_{\mathrm{sw}})\rvert - \lvert Z_{\mathrm{DS}}(3w_{\mathrm{sw}})\rvert$	6.53 dB	7.15 dB	5.87 dB
$\angle Z_{DS}(\omega_{sw})$	48.84 deg	52.76 deg	43.21 deg
$\angle Z_{DS}(3\omega_{sw})$	-84.66 deg	-85.32 deg	-83.61 deg

-80 degrees.

Three experiments result in the average power output, maximum V_{DS}, and efficiency of the inverter from the component tuning process in Table 5.1. The table includes the Class Φ_2 inverter design parameters of L_F, C_P, and C_P, considering with C_{OSS} in the simulation. As you can see, three circuit designs can achieve the criteria for ZVS operation. While the maximum V_{DS} provides the lowest value, causing the lowest switching loss, the efficiency of this case is the lowest compared to other cases. Otherwise, the output power in Case 3 cannot achieve the 300-W power requirement. Moreover, it provides the highest maximum V_{DS}, leading to high switching loss. Therefore, Case 1 is selected due to its high efficiency and medium maximum V_{DS}, including the ability to give 300-W output power.

The selected optimal components of Class Φ_2 inverter operating in ZVS condition for 300 W of the power with 160 V of DC input voltage in 13.56-MHz frequency, represented in Fig. 5.1.

From the simulation of Class Φ_2 inverter, we can capture the V_{DS} waveform the V_{DS} waveform can be captured in the bottom subplot in Figure 5.3. It shows the operation at ZVS condition with its peak voltage at 342.43 V, around two times the input voltage when R_L is 50 Ω. Also, the output voltage waveform at the top of Figure 5.3 is the closely sinusoidal shape for the AC output inverter.

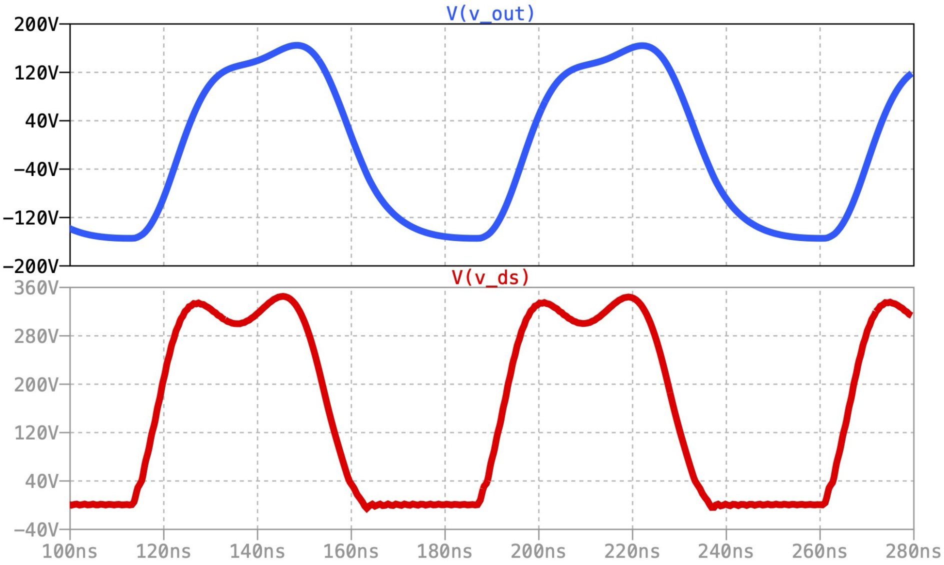

Figure 5.3: Simulation and waveforms of V_{DS} and V_{out}.

Table 5.2: Parameter Setup of ANSYS Simulation.

Parameter Setup	**Value**
Solution selection	R_s, X_s
Maximum Number of Passes	15
Minimum Number of Passes	1
Minimum Converged Number of Passes	3
Maximum Delta Z_o	2%
Maximum Refinement Per Pass	30%

5.2 13.56 MHz Double-Layer Planar Spiral Coil Design

ANSYS Maxwell will be used as the software to design and simulate the coil for WPT. The initial attempt was to create a two-layer spiral coil and get the value of resistance and reactance of the coil from the Z-parameter. Figure 5.4 and Table 5.3 show ANSYS's coil 3D design and design parameters. With a simulation setup as represented in Table 5.2, we can simulate the solution in approximately 2-5 minutes for each coil design simulation.

5.2.1 Quality Factor of the Optimized Coil Design using Machine Learning

To produce quality factors from the Z-parameter in the simulation, we can extract the reactance (X_{sim}) and resistance (R_{sim}) of the Z-parameter. These parameters are applied to calculate the Q-factor (Q_{sim}) by solving L_{sim} and C_{sim} from two equations:

$$\begin{aligned} \omega_1 L_{sim} - \frac{1}{\omega_1 C_{sim}} - X_{sim,1} = 0, \\ \omega_2 L_{sim} - \frac{1}{\omega_2 C_{sim}} - X_{sim,2} = 0. \end{aligned} \tag{5.1}$$

The result of L_{sim} is the initial parameter for calculating Q_{sim} including R_{sim} from:

$$Q_{sim} = \frac{\omega_1 L_{sim}}{R_{sim}}, \tag{5.2}$$

where $\omega_1 = 2\pi F_{sw}$ is the operating resonant frequency and ω_2 is denoted as a frequency with a small difference from the operating resonant frequency, which assists in deriving the Q-factor. For example, the simulation provides the resistance of 187.5287 and 187.5384 $m\Omega$ at 13.56 MHZ and 13.561 MHz, and an 84.224-Ω reactance and an 84.2455-Ω reactance with the respective frequencies, based on the design parameters, as shown in Table 5.3. The results of solving Eq. (5.1) are a 2.2146-μH inductance and a 112.4422-pF capacitance. Next, we determine Q_{sim} of 1005.75 by using Eq. (5.2) at 13.56 MHz frequency. Based on optimizing the coil design using machine learning at 13.56 MHz frequency, the highest Q is 1005.75 with the given design requirements in Table 5.3. In addition, the design of a nonuniform two-layer spiral coil is demonstrated in Figure (5.4).

5.2.2 Quality Factor of Coil Design Experiments

Since we have the optimized coil design with the highest Q, the 200-mm coil design is built from a 0.5-mm copper sheet in a physical structure, as demonstrated in Fig. 5.5. In this study, a water-jet machine cuts the coil in the proposed spiral shape. The first layer has a total diameter of 20 cm with a 13.87-mm width and

Table 5.3: Two-layer spiral coil geometric parameters.

Geometric Parameters	**Values**
$Freq$	13.56 MHz
N	4
d	2.372 mm
D_{o1}	200 mm
D_{o2}	200 mm
D_{i1}	50 mm
D_{i2}	50 mm
w_1	13.87 mm
w_2	15.06 mm
t_1	0.5 mm
t_2	0.5 mm
R_{sim}	187.528 $m\Omega$
X_{sim}	84.224 Ω
L_{sim}	2.215 μH
Q	1005.75

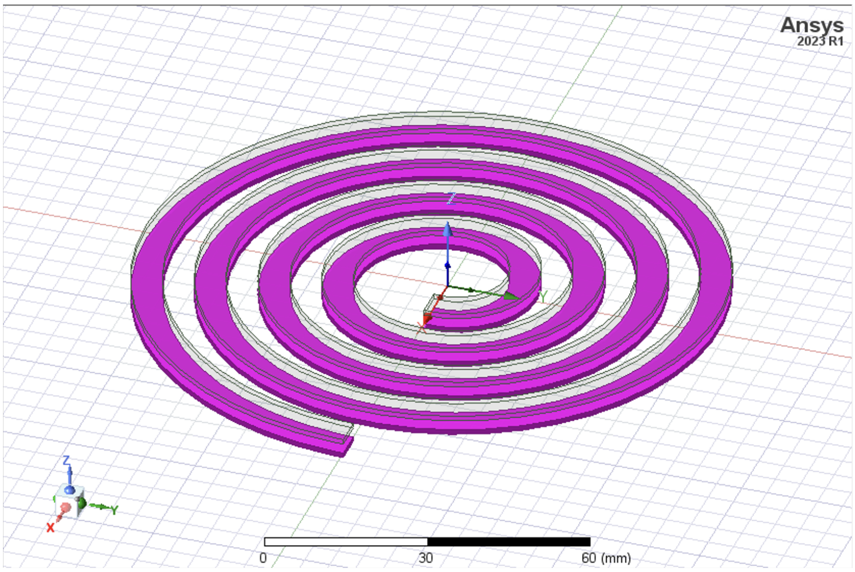

Figure 5.4: Uniform two-layer planar spiral coil design.

a 5 cm inner diameter. The coil is assembled in two layers without any contact. They were set up with a 2.37-mm air gap between the layers held by acrylic sheets. The performance of the physical high-frequency resonant coil is indicated with Q-factor values, derived by measuring the Z-parameter, resistance, inductance, and capacitance of the Network Analyzer in various sweep frequencies.

As you can see in Fig. 5.6, the Z-parameter of this design can be measured at 52.233 Ω at 13.56 MHz with a 365.62-Ω resistance. The quality factor is calculated,

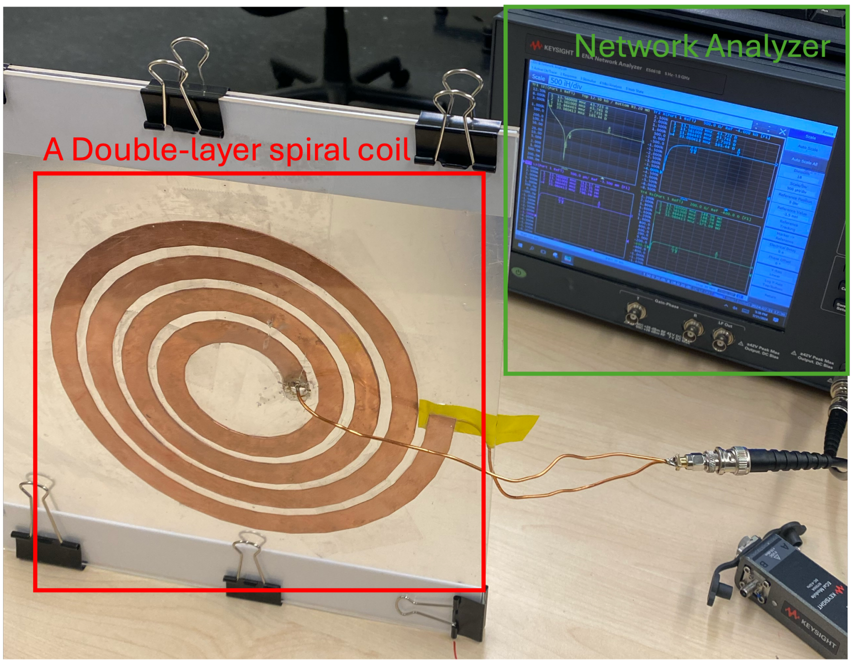

Figure 5.5: A double-layer spiral coil experiment setup.

accounting for 551.31. However, this design's resonant frequency at 10.63 MHz is noticeably lower than the desired resonant frequency at 13 MHz. Adjusting the distance between the coil, d, from 2.37 mm to 3.38 mm, results in a 13-MHz resonant frequency performance with 777.53 Q-factor to achieve the desired frequency. This new design performs with 870.04 of coil reactance and 598.01 mΩ of coil resistance at 13.56 MHz. The frequency sweep of this design is shown in Fig. 5.7. To conclude, the 3.38-mm distance between two layers of coil design produces a higher Q value with lower resistance and reactance because of its ability to perform in operating resonant frequency at 13.56MHz in this study.

5.2.3 Comparison of Simulation-based, ML-based and Physical Experiments

Q-factor generation from simulation, ML-based coil optimization results in Table 5.4. As you can see, the coil design from the machine learning method performs 963.27 with 4.22% error from the simulation. However, the Q-factor of the coil in the actual setup drops to 551.31 with a 45.18 % error. This is because of the lack of resonant performing capability in the Experiment 1. After adjusting the gap distance to 3.38

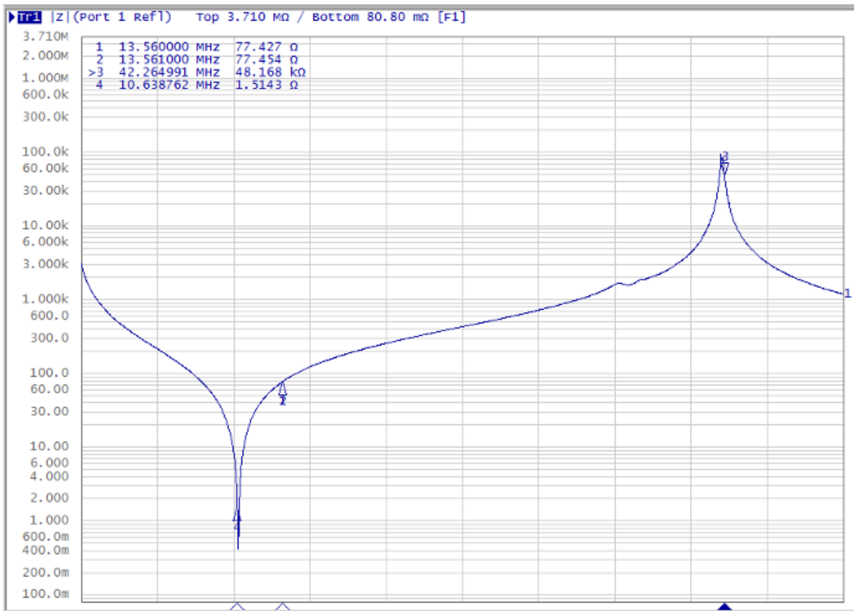

```
Tr1 |Z|(Port 1 Refl)   Top 3.710 MΩ / Bottom 80.80 mΩ [F1]
  1  13.560000 MHz  77.427 Ω
  2  13.561000 MHz  77.454 Ω
 >3  42.264991 MHz  48.168 kΩ
  4  10.638762 MHz  1.5143 Ω
```

Figure 5.6: Magnitude of Z-parameter frequency sweep in the coil design of 2.37-mm of *d*.

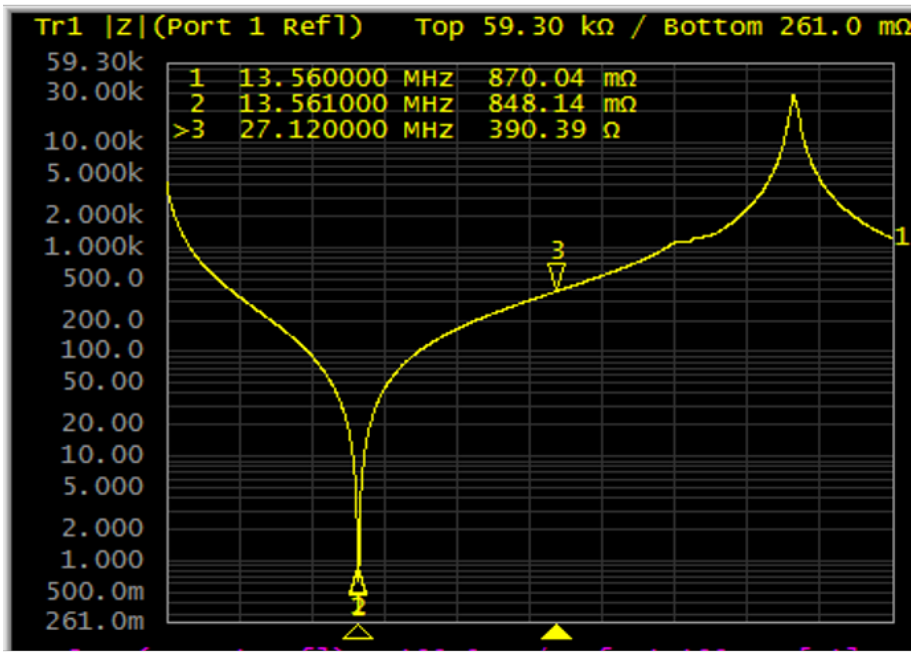

```
Tr1 |Z|(Port 1 Refl)   Top 59.30 kΩ / Bottom 261.0 mΩ
  1  13.560000 MHz  870.04 mΩ
  2  13.561000 MHz  848.14 mΩ
 >3  27.120000 MHz  390.39 Ω
```

Figure 5.7: Magnitude of Z-parameter frequency sweep in the coil design of 3.38-mm of *d*.

mm, Experiment 2 shows a 989 Q-factor performance in the simulation, which can be performed at the resonant 13.56-MHz frequency. Comparing the Q factor of the simulation and ML-based, In the same manner, the physical resonant coil generates Q lower than the simulation, and ML-based Q estimation accounts for 777.53, which has an error of around 21.38% compared to simulation Q production. The reduction

Table 5.4: Optimization Results of a double-layer planar spiral coil designs.

Optimization Results	Experiment 1 (d = 2.37 mm)			Experiment 2 (d = 3.38 mm)		
	ML-based	Simulation	Physical Coil	ML-based	Simulation	Physical Coil
Quality Factor	**963.27**	**1005.75**	**551.31**	**987.41**	**989.00**	**777.53**
Error with simulation	**4.22%**	**-**	**45.12%**	**0.16%**	**-**	**21.38%**
Operating Time (min)	**0:53**	**1:41**	**-**	**0:58**	**2:25**	**-**
F_{sw} (MHz)	13.56			13.56		
D_{o1} (mm)	200			200		
D_{o2} (mm)	200			200		
w_1 (mm)	13.87			13.87		
w_2 (mm)	15.06			15.06		
D_{i1} (mm)	50			50		
D_{i2} (mm)	50			50		
N	4			4		
d (mm)	2.37			3.38		
p_1 (mm)	7.06			7.06		
p_2 (mm)	5.46			5.46		
t_1 (mm)	0.5			0.5		
t_2 (mm)	0.5			0.5		

of Q occurs because of the resistance of the cable and soldering connection, including the conduction losses in the actual setup, which consequently produce a lower quality factor [10]. However, the simulation and ML-based Q results in Experiment 2 have a slight difference, accounting for 0.16%, meaning that the machine learning method evaluates the Q-factor precisely and satisfies better time-consumption in simulation by saving 1.27 minutes from 2.30 minutes per simulation.

Chapter 6

Conclusion and Future Work

This study presents the optimization of the proposed spiral coil design in high-frequency wireless power transfer systems using machine learning methods. To transfer high-efficiency power, the coil performs with a Class Φ_2 inverter. First, a Class Φ_2 inverter was selected for the WPT system, operating under Zero Voltage Switching (ZVS) conditions at 300 W power with an efficiency of 99.25% in the simulation setup. A proposed double-layer SR coil design was simulated to analyze the resistance and impedance, achieving a Q-factor of 989, the highest recorded with the given design parameters. Also, the proposed ML-based coil optimization predicts 987.41, which considers low error, accounting for only a 0.16% difference from the simulation. However, the physical experiment coil sufficiently achieves 777.53 of Q because of the unavoidable resistance from cable and conduction losses. We implemented a machine learning-based method to achieve the optimization process and high-quality factors, significantly reducing the time required for each simulation to a few seconds in this paper. This approach demonstrates the potential of machine learning in advancing the design and efficiency of high-frequency coil design in WPT systems.

Despite this, one observation is that to enhance the model's performance, more data should be collected. It is also important that the optimization process is essential to further improve for offering even high Q and optimal coil designs achieving at resonant frequencies. However, optimizing with these new constraints is challenging due to the strict requirements for resonant frequency operation. Therefore, future studies should improve the optimization method to include resonant conditions to achieve optimization at the desired frequency. This will ensure the optimal outcome by satisfying both resonant operation and design constraints, achieving an optimal Q factor and other design parameters.

Bibliography

[1] G. Longobardi, "GaN for power devices: Benefits, applications, and normally-off technologies," 2017 International Semiconductor Conference (CAS), Sinaia, Romania, 2017, pp. 11-18, doi: 10.1109/SMICND.2017.8101144.

[2] J. Choi, D. Tsukiyama, Y. Tsuruda, and J. M. R. Davila, "High-Frequency, High-Power Resonant Inverter With eGaN FET for Wireless Power Transfer," in IEEE Transactions on Power Electronics, vol. 33, no. 3, pp. 1890-1896, March 2018, doi: 10.1109/TPEL.2017.2740293.

[3] J. M. Rivas, Y. Han, O. Leitermann, A. D. Sagneri and D. J. Perreault, "A High-Frequency Resonant Inverter Topology With Low-Voltage Stress," in IEEE Transactions on Power Electronics, vol. 23, no. 4, pp. 1759-1771, July 2008, doi: 10.1109/TPEL.2008.924616.

[4] GaN Systems, "GS66508T Top-side cooled 650 V E-mode GaN transistor," GS66508T datasheet, Rev. 200402.

[5] I. Sasahara and K. Akatsu, "A Coupler design for high power 2.3 kW WPT using 13.56 MHz," 2022 IEEE 31st International Symposium on Industrial Electronics (ISIE), Anchorage, AK, USA, 2022, pp. 762-767, doi: 10.1109/ISIE51582.2022.9831577.

[6] M. Kim and J. Choi, "Design of Self-Resonant Spiral Coils for Mid-Range, High-frequency Wireless Power Transfer Systems," 2022 Wireless Power Week (WPW), Bordeaux, France, 2022, pp. 33-38, doi: 10.1109/WPW54272.2022.9853905.

[7] J. Li and D. Costinett, “Analysis and design of a series self-resonant coil for wireless power transfer,” 2018 IEEE Applied Power Electronics Conference and Exposition (APEC), San Antonio, TX, USA, 2018, pp. 1052-1059, doi: 10.1109/APEC.2018.8341145.

[8] R. Qin, J. Li and D. Costinett, “A 6.6-kW High-Frequency Wireless Power Transfer System for Electric Vehicle Charging Using Multilayer Nonuniform Self-Resonant Coil at MHz,” in IEEE Transactions on Power Electronics, vol. 37, no. 4, pp. 4842-4856, April 2022, doi: 10.1109/TPEL.2021.3120734.

[9] M. Kim, M. Jeong, M. Cardone and J. Choi, “Optimization of Spiral Coil Design for WPT Systems using Machine Learning,” 2023 IEEE Applied Power Electronics Conference and Exposition (APEC), Orlando, FL, USA, 2023, pp. 822-828, doi: 10.1109/APEC43580.2023.10131149.

[10] M. Kim, M. Jeong, M. Cardone, and J. Choi, “Design of a Spiral Coil for High-Frequency Wireless Power Transfer Systems Using Machine Learning,” in *IEEE Journal of Emerging and Selected Topics in Industrial Electronics*, vol. 5, no. 1, pp. 193-202, Jan. 2024, doi: 10.1109/JESTIE.2023.3317797.

[11] P. K. Chittoor, B. Chokkalingam, and L. Mihet-Popa, “A Review on UAV Wireless Charging: Fundamentals, Applications, Charging Techniques and Standards,” IEEE Access, vol. 9, pp. 69235–69266, 2021, doi: 10.1109/access.2021.3077041.

[12] C. Rong et al., “Critical Review of Recent Development of Wireless Power Transfer Technology for Unmanned Aerial Vehicles,” in IEEE Access, vol. 11, pp. 132982-133003, 2023, doi: 10.1109/ACCESS.2023.3332470.

[13] “Unmanned Aerial Vehicle Market, UAV Size, Share, system and Industry Analysis and Market Forecast to 2024 — MarketsandMarketsTM,” Marketsandmarkets.com, 2019. Accessed: Jul. 1, 2024. [Online.] Avail-

able: https://www.marketsandmarkets.com/Market-Reports/unmanned-aerial-vehicles-uav-market-662.html

[14] A. Iqbal and S. Aftab, “A Feedforward and Pattern Recognition ANN Model for Network Intrusion Detection,” International Journal of Computer Network and Information Security, vol. 14, pp. 19, 2019, doi: 10.5815/ijcnis.2019.04.03.

[15] S. D. Barman, A. W. Reza, N. Kumar, Md. E. Karim, and A. B. Munir, “Wireless powering by magnetic resonant coupling: Recent trends in wireless power transfer system and its applications,” Renewable and Sustainable Energy Reviews, vol. 51, pp. 1525–1552, Nov. 2015, doi: https://doi.org/10.1016/j.rser.2015.07.031.

[16] C. Jiang, K. T. Chau, C. Liu, and C. H. T. Lee, “An Overview of Resonant Circuits for Wireless Power Transfer,” Energies, vol. 10, no. 7, p. 894, Jun. 2017, doi: 10.3390/en10070894.

[17] D. Patil, M. K. McDonough, J. M. Miller, B. Fahimi and P. T. Balsara, “Wireless Power Transfer for Vehicular Applications: Overview and Challenges,” in IEEE Transactions on Transportation Electrification, vol. 4, no. 1, pp. 3-37, March 2018, doi: 10.1109/TTE.2017.2780627.

[18] J. Millán, P. Godignon, X. Perpiñà, A. Pérez-Tomás, and J. Rebollo, “A Survey of Wide Bandgap Power Semiconductor Devices,” in IEEE Transactions on Power Electronics, vol. 29, no. 5, pp. 2155-2163, May 2014, doi: 10.1109/TPEL.2013.2268900.

[19] X. She, A. Q. Huang, Ó. Lucía, and B. Ozpineci, “Review of Silicon Carbide Power Devices and Their Applications,” in IEEE Transactions on Industrial Electronics, vol. 64, no. 10, pp. 8193-8205, Oct. 2017, doi: 10.1109/TIE.2017.2652401.

[20] E. A. Jones, F. F. Wang, and D. Costinett, “Review of Commercial GaN Power Devices and GaN-Based Converter Design Challenges,” in IEEE Jour-

nal of Emerging and Selected Topics in Power Electronics, vol. 4, no. 3, pp. 707-719, Sept. 2016, doi: 10.1109/JESTPE.2016.2582685.

[21] E. Noh, J. So, and S. -H. Lee, “Machine-Learning Based Optimal Design of a Wireless Power Transfer Coil for Battery-Powered Tram,” 2023 11th International Conference on Power Electronics and ECCE Asia (ICPE 2023 - ECCE Asia), Jeju Island, Korea, Republic of, 2023, pp. 1867-1872, doi: 10.23919/ICPE2023-ECCEAsia54778.2023.10213852.

[22] S. Inoue et al., “Fast Design Optimization Method Utilizing a Combination of Artificial Neural Networks and Genetic Algorithms for Dynamic Inductive Power Transfer Systems,” in IEEE Open Journal of Power Electronics, vol. 3, pp. 915-929, 2022, doi: 10.1109/OJPEL.2022.3224422.

[23] F. Emmert-Streib, Z. Yang, H. Feng, S. Tripathi, M. Dehmer, “An Introductory Review of Deep Learning for Prediction Models With Big Data,” Front Artif Intell, Feb. 2020, doi: 10.3389/frai.2020.00004.

[24] Nwankpa CE, Ijomah W, Gachagan A, and Marshall S. “Activation functions: comparison of trends in practice and research for deep learning,” 2nd International Conference on Computational Sciences and Technology, Jamshoro, Pakistan, 2021, doi: 10.48550/arXiv.1811.03378.

[25] H. Zhang, M. Liao, L. He, and C. K. Lee. “Parameter Optimization of Wireless Power Transfer Based on Machine Learning,” *Electronics.* 2024; 13(1):103. doi: 10.3390/electronics13010103.

[26] H. Lee, Y. Kim, S. Yang, and H. Choi, “Improved weight initialization for deep and narrow feedforward neural network, Neural Networks,” Volume 176, 2024, 106362, ISSN 0893-6080, doi: 10.1016/j.neunet.2024.106362.

[27] Choi, R. Y., Coyner, A. S., Kalpathy-Cramer, J., Chiang, and M. F., & Campbell, J. P, “Introduction to Machine Learning, Neural Networks, and Deep

Learning," Translational vision science & Technology, 9(2), 14, Feb. 2020, doi: 10.1167/tvst.9.2.14.

[28] J. Ming, F. Taip, M. S.Anuar, S. Noor, and Z. Abdullah, "Artificial Neural Network Topology Optimization using K-Fold Cross Validation for Spray Drying of Coconut Milk," IOP Conference Series: Materials Science and Engineering, 778, 012094, 2020, doi:10.1088/1757-899X/778/1/012094.

[29] T. Guillod, P. Papamanolis, and J. W. Kolar, "Artificial Neural Network (ANN) Based Fast and Accurate Inductor Modeling and Design," in IEEE Open Journal of Power Electronics, vol. 1, pp. 284-299, 2020, doi: 10.1109/OJPEL.2020.3012777.

[30] Beal, L.D.R., Hill, D., Martin, R.A., and Hedengren, J. D., "GEKKO Optimization Suite," Processes, Volume 6, Number 8, 2018, doi: 10.3390/pr6080106.